DESIGN AND EVALUATION OF A THERMAL NOZZLE FOR SMALL-SCALE TURBOJETS

By
JOSHUA ROBERT BRAUN

Bachelor of Science in Engineering
Oral Roberts University
Tulsa, OK
2020

Submitted to the Faculty of the
Graduate College of the
Oklahoma State University
in partial fulfillment of
the requirements for
the Degree of
MASTER OF SCIENCE
May, 2022

DESIGN AND EVALUATION OF A
THERMAL NOZZLE FOR
SMALL-SCALE TURBOJETS

Thesis Approved:

Dr. Rouser

Thesis Advisor

Dr. Jacob

Dr. Bradshaw

Name: JOSHUA ROBERT BRAUN

Date of Degree: MAY, 2022

Title of Study: DESIGN AND EVALUATION OF A THERMAL NOZZLE FOR SMALL-SCALE TURBOJETS

Major Field: MECHANICAL & AEROSPACE ENGINEERING

Abstract: This paper presents the design and evaluation of a thermal nozzle for small-scale turbojets. Historically, small-scale turbojets have suffered from poor thermal efficiency and thrust specific fuel consumption (TSFC). This is primarily because their small geometry limits the compressor pressure ratio from reaching higher values, which directly impacts TSFC. An alternative approach to improving TSFC is to preheat the fuel before it enters the combustion chamber. This will add enthalpy to the flow, thus reducing the amount of fuel required to the reach the same turbine inlet temperature. The thermal nozzle presented in this study achieves this by acting as a heat exchanger between the hot exhaust gas and the fuel before it enters the engine.

Computational fluid dynamics (CFD) and preliminary experiments were used to guide the design of the nozzle, where key considerations included pressure drop, fuel temperature limits, and manufacturability. Parameters such as channel geometry and thickness were varied and analyzed to arrive at a final design that met the design goals. A 70 lbf KingTech K320 turbojet was chosen to evaluate the performance of the thermal nozzle. Analytical evaluation was performed using an ε-NTU heat exchanger model calibrated from CFD results, parametric cycle analysis, and engine performance analysis. Analysis shows a TSFC improvement of 2.07% at full throttle. However, the heat that is recuperated in the nozzle slightly reduces the thrust output of the engine, where analysis for specific thrust shows a decrease of 0.48% at full throttle.

TABLE OF CONTENTS

LIST OF TABLES

LIST OF FIGURES

CHAPTER I

INTRODUCTION

1.1 Motivation

Small-scale turbojets, which can be defined as those producing less than 1,000 lbs of thrust [28, 27], are prone to short mean time between overhaul (MTBO) and low thermal efficiency, which leads to increased thrust specific fuel consumption (TSFC) [31, 25]. This low thermal efficiency is primarily the result of low compressor pressure ratios, as demonstrated by their relationship in Fig. 1 and Eqn. 1.1.1 (ideal, static equation). Having a higher compressor pressure ratio better prepares the air for combustion, thus increasing the burner efficiency and thermal efficiency. However, improvement of the pressure ratio is constrained by the small geometry of the turbojet, where viscous boundary layer effects begin to dominate the small airflow volume and restrict further compression.

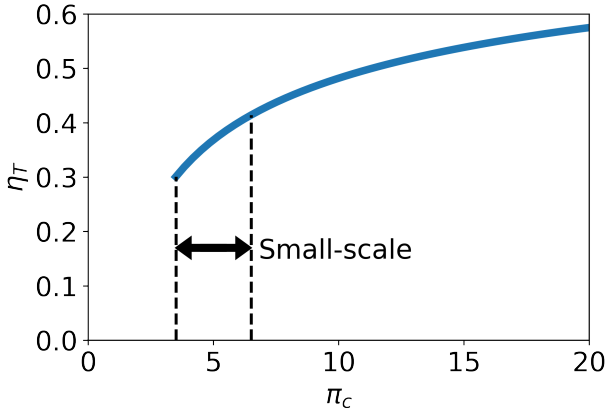

Figure 1: Thermal efficiency, η_T, vs. compressor pressure ratio, π_c

$$\eta_T = 1 - \frac{1}{\pi_c^{\frac{\gamma-1}{\gamma}}} \tag{1.1.1}$$

1.2 Proposed Solution

Aside from increasing the compressor pressure ratio, another potential method to improve thermal efficiency is to preheat the fuel entering the combustion chamber, as it is well-recognized that heating any of the combustion reactants improves the overall combustion efficiency [29]. Additionally, because the heat of combustion is a function of reactant temperature, it could also be elevated by preheating the fuel, allowing more energy to be extracted from the fuel.

While fuel is routinely preheated on large-scale aircraft, this has not been done on small-scale turbojets. One potential method to achieve this in small-scale applications is to route the fuel through a thermal nozzle, which recuperates heat from the hot exhaust gases to preheat the fuel for combustion. This device, sketched in Fig. 2, would involve a simple retrofit to an existing engine that would not require the engine to be opened up at all. The preheated fuel obtained by this nozzle should improve burner efficiency, thus improving thermal efficiency and TSFC.

Additionally, it is possible that this device can improve in-flight restart reliability because of the additional enthalpy in the fuel. Mean time between overhaul could potentially be improved as the need for vaporization tubes within the engine is reduced, where the temperature of the fuel can be controlled more easily with the thermal nozzle to reduce fuel coking.

1.3 Objectives

This study will follow the design of a thermal nozzle and evaluation of its performance when additively manufactured in Haynes 282 and installed on a 70 lbf KingTech K320 turbojet. Jet A and diesel will be used in the evaluation at a range of fuel flow rates, from idle to full

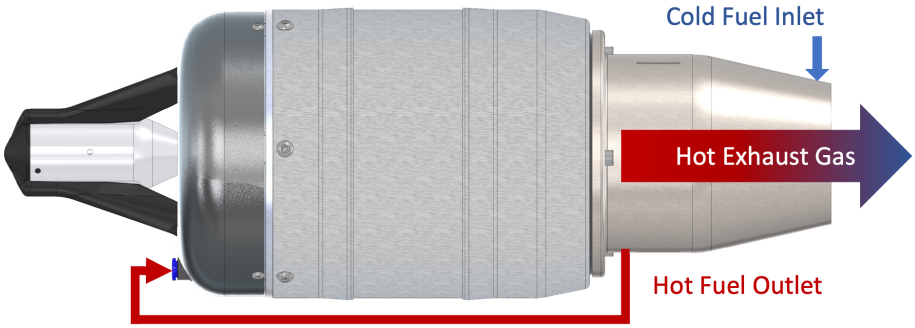

Figure 2: Schematic of the proposed thermal nozzle concept

throttle. At each throttle setting, the fuel flow rate, thrust output, and fuel temperature at the nozzle exit will be measured. From these quantities, TSFC can be calculated as the key output metric. Testing over this range of input parameters will reveal the effects of the thermal nozzle on thrust and TSFC at varying operating points and whether an optimal operating point exists.

CHAPTER II

BACKGROUND

A schematic of a typical jet engine is shown in Fig. 3, where the station numbers will be used throughout the fundamental theory.

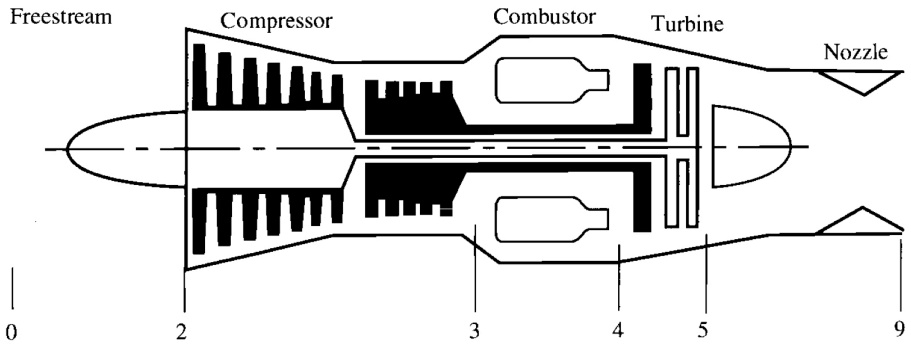

Figure 3: Station numbering for a jet engine [21].

2.1 Fundamental Theory

Poor thermal efficiency, η_T, leads to an increase in TSFC, as seen in Eq. 2.1.2 [21]. Thermal efficiency is defined as the net rate of work output by the turbine divided by the rate of heat input to the system from the burner, which can also be written in terms of engine properties and operational parameters (Eq. 2.1.1 [21]).

$$\eta_T = \frac{\dot{W}_{out}}{\dot{Q}_{in}} = 1 - \frac{1}{\pi_r^{\frac{\gamma-1}{\gamma}} \pi_c^{\frac{\gamma-1}{\gamma}}} = \frac{(1+f)V_9^2 - V_0^2}{2g_c f h_{PR}} \tag{2.1.1}$$

$$TSFC = \frac{V_0}{\eta_P \eta_T h_{PR}} = \frac{(1+f)V_9^2 - V_0^2}{2g_c(F/\dot{m}_0)\eta_T h_{PR}} = \frac{f\dot{m}_0}{F} = \frac{\dot{m}_f}{F} \tag{2.1.2}$$

where $\dot{W}_{out}$ is the work output of the turbine, $\dot{Q}_{in}$ is the heat input to the burner, $\pi_r = (P_{t0}/P_0) = 1$ for this study because a static test stand is used, f is the fuel-to-air ratio, V_i is the velocity at station i, g_c is a proportionality constant, h_{PR} is the fuel's heat of combustion, η_P is the propulsive efficiency, F is the thrust output, $\dot{m}_0$ is the air mass flow rate, and $\dot{m}_f$ is the fuel mass flow rate.

In these equations, the compressor pressure ratio, π_c, is constrained by the engine geometry, and other parameters can be assumed to be relatively constant. It is clear from these relations that for a given thrust, TSFC is ultimately governed by $\dot{m}_f$, which is defined as [21]:

$$\dot{m}_f = \frac{\dot{m}_0(c_{p,t}T_{t4} - c_{p,c}T_{t3})}{\eta_b h_{PR} - c_{p,t}T_{t4}} \tag{2.1.3}$$

where $c_{p,t}$ and $c_{p,c}$ are the specific heat capacities of air on the turbine and compressor sides of the burner respectively, T_{t3} is the temperature at the burner inlet, T_{t4} is the temperature at the burner outlet, and η_b is the burner efficiency. The thermal nozzle will add enthalpy to the flow, $\dot{Q}_{f,noz}$, which enters the $\dot{m}_f$ relationship as follows:

$$\dot{m}_f = \frac{\dot{m}_0(c_{p,t}T_{t4} - c_{p,c}T_{t3}) - \dot{Q}_{f,noz}}{\eta_b h_{PR} - c_{p,t}T_{t4}} \tag{2.1.4}$$

Clearly, increasing the heat transfer to the fuel will reduce the $\dot{m}_f$ required to reach a certain T_{t4}. While removing the heat from the exhaust gas will reduce the thrust output of the engine, later analysis will show that there is a net benefit to TSFC.

Additionally, literature has shown that increasing the fuel inlet temperature should increase η_b. Simple analysis of h_{PR} shows this quantity is also increased with increasing fuel inlet temperature. Increasing either η_b or h_{PR} improves η_T and, in turn, TSFC. This relationship is demonstrated by Fig. 4.

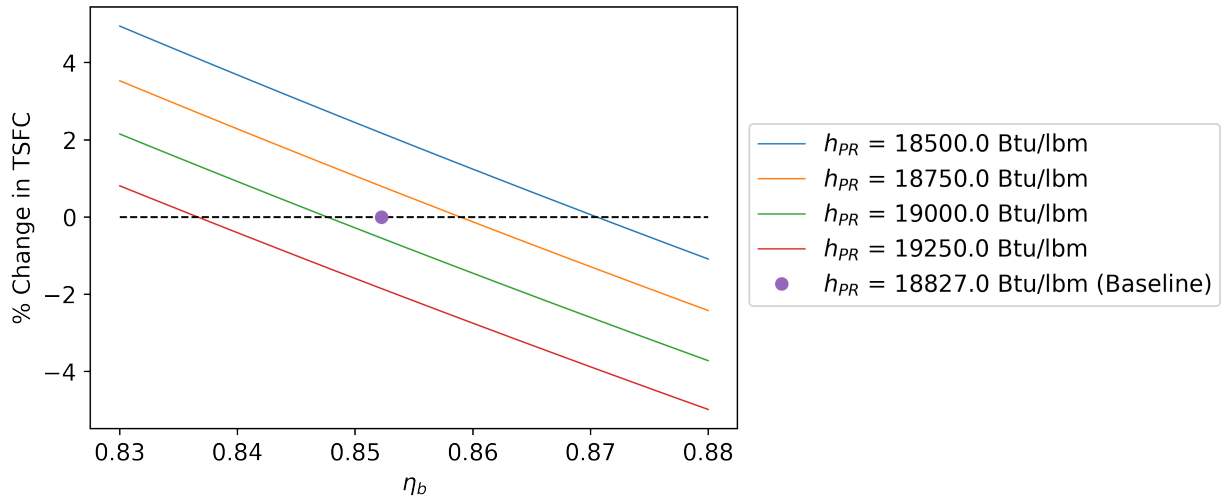

Figure 4: Effect of η_b and h_{PR} on TSFC. While KingTech K320 cycle values are used, the trends are not unique to this engine.

2.1.1 Heat of Combustion

The heat of combustion, H_{PR}, is the heat released during a combustion reaction, which is equal to the enthalpy of the reactants at the initial temperature, $H_R(T_0)$, minus the enthalpy of the products after they have been cooled to that same temperature, $H_P(T_0)$ [19, Ch. 13.3.3]:

$$H_{PR} = H_R(T_0) - H_P(T_0) = \sum_R H_i(T_0) - \sum_P H_j(T_0) \tag{2.1.5}$$

where i and j denote the chemical components of the reactants and products respectively. In parametric cycle analysis, which is examined in a later section, heat of combustion is used on a per-unit-mass basis, denoted h_{PR}.

The previous equation shows that heat of combustion is dependent on the temperature of the reactants entering the combustion chamber. To calculate the standardized molar specific enthalpy of each component i, Eq. 2.1.6 is used, which corresponds to the enthalpy of formation plus the enthalpy departure from standard state conditions [19, Eq. 13-50]:

$$\bar{h}_{i,std}(T_0, P_0) = \bar{h}_{i,form} + \left[\bar{h}_i(T_0, P_0) - \bar{h}_i(T_{ref}, P_{ref})\right] \tag{2.1.6}$$

Because the heat of combustion plays a direct role in the heat added to the engine in the burner and is dependent on the temperature of the reactants, this discussion will become important when analyzing the impact of fuel preheating on the engine cycle analysis (section 2.1.6).

Determining Changes in h_{PR}

EES (Engineering Equation Solver) is a useful tool to analyze changes in h_{PR} because of its thermo-physical libraries, equation solvers, and handling of units. While Jet A and diesel are not included in the libraries, they can be approximated by a type of kerosene called n-Dodecane ($C_{12}H_{26}$), where a comparison of enthalpies of formation is given by Table 1.

Table 1: Comparison of different fuels

	n-Dodecane [24]	Jet A [21]	Diesel
Enthalpy of formation (Btu/lbmol)	-150,172	-152,981	-*

* Value is unavailable because there is not a single chemical definition for diesel [7]. Rather, it is a family of fuels similar to kerosene.

The stoichiometric equation for combustion of n-Dodecane is given by:

$$C_{12}H_{26} + 18.5(O_2 + 3.76N_2) \rightarrow 12CO_2 + 13H_2O + 69.56N_2 \tag{2.1.7}$$

Because $\dot{m}_{air}$ is much higher than $\dot{m}_f$ entering the combustor, it can be assumed that T_0 in Eq. 2.1.5 is equal to T_{air}, except for the fuel component, which will be T_f coming from the thermal nozzle.

When carrying out this analysis in EES, certain assumptions are made:

- The temperature and pressure of the reactants and products (except the fuel temperature) are equal to T_{t3} and P_{t3} respectively.
- The temperature of the fuel entering the combustion chamber is T_f.
- O_2, N_2, CO_2, and H_2O are modeled as ideal gases.

- $\bar{h}_{form,C_{12}H_{26}} = -150,172$ Btu/lbmol [24]

2.1.2 Adiabatic Flame Temperature

The steady state energy balance for a combustion process is given by [19, Ch. 13.3.5]:

$$H_R = Q_{out} + H_P \tag{2.1.8}$$

The adiabatic flame temperature, T_{ad}, is defined as the temperature of the combustion products when there is no heat transfer to the surroundings. Rearranging Eq. 2.1.8 after setting $Q_{out} = 0$ gives:

$$H_{R,T_0} = H_{P,T_{ad}} \tag{2.1.9}$$

As discussed in the previous section, increasing the fuel reactant temperature will increase its enthalpy. With a higher H_{R,T_0}, T_{ad} will also increase for $H_{P,T_{ad}}$ to match. When finding T_{ad} in EES, the same assumptions are used as for finding the heat of combustion.

2.1.3 Heat Transfer

Heat transfer is the fundamental physics phenomenon at work in the thermal nozzle. This topic can generally be broken down into three main mechanisms of heat transfer: radiation, conduction, and convection. Because the exhaust gas does not emit radiation and the net radiation heat transfer between nozzle surfaces is negligible, radiation will be ignored. The more prominent heat transfer mechanisms are forced convection and conduction. Convection occurs between the air and the nozzle and between the nozzle and the fuel, while conduction occurs throughout the nozzle material.

Convection

Convection is heat transfer that occurs by fluid motion and a temperature difference between a surface and the fluid. Forced convection occurs when the fluid is in motion and in contact with a surface at a different temperature. Natural convection occurs when a static fluid is in contact with a surface at a different temperature, where the heat transferred at the surface by conduction causes density changes in the fluid that induce motion by buoyancy effects. In the case of the thermal nozzle, forced convection is at work with hot air rushing through the nozzle and fuel flowing through the nozzle channels.

In general, convection is described by Newton's law of cooling [34]:

$$\dot{Q}_{conv} = hA_s(T_s - T_\infty) \tag{2.1.10}$$

where $\dot{Q}_{conv}$ is the rate of heat transfer by convection, h is the convection heat transfer coefficient, A_s is the surface area in contact with the fluid, T_s is the surface temperature, and T_∞ is the free stream fluid temperature. The convection heat transfer coefficient can be difficult to determine because it is highly dependent on the geometry of the surface and the direction of the flow. It is common practice to non-dimensionalize the convection coefficient with the Nusselt number, defined by [34]:

$$Nu = \frac{hL_c}{k} \tag{2.1.11}$$

where L_c is the characteristic length and k is the thermal conductivity of the fluid. Many Nusselt number correlations have been empirically determined for a variety of geometries, which are typically grouped into internal and external flows.

Usually, these correlations depend on fluid properties at a certain temperature (which depends on the case) and the Reynolds number of the flow. Typically, higher Reynolds numbers correspond to higher Nusselt numbers and, by extension, higher convection heat transfer coefficients. An example of this correlation is shown by the Dittus-Boelter equation

for turbulent, internal forced convection [34]:

$$Nu = 0.023 Re^{0.8} Pr^{n} \tag{2.1.12}$$

where Re is the Reynolds number, Pr is the Prandtl number (fluid property), and $n = 0.4$ for heating and $n = 0.3$ for cooling of the fluid. The Reynolds number correlation will be used in Section 3.2 to perform simple analysis on the relationship between channel geometry and convection heat transfer coefficient.

Correlations for Nusselt numbers are highly dependent on the geometry of the problem. Because the thermal nozzle geometry is unique, analytical results will not be carried out. Rather, the computational fluid dynamics (CFD) program, Star-CCM, will model the flow of exhaust gas through the nozzle and fuel through the fuel channels, and a discretized, finite volume solution for convective heat transfer will be obtained.

Conduction

Conduction is the transfer of heat through a medium, whether that be a fluid or a solid. The rate at which this occurs is governed by Fourier's law of heat conduction:

$$\dot{Q}_{cond} = -kA\frac{dT}{dx} \tag{2.1.13}$$

where k is the thermal conductivity of the medium, A is the conduction area, and dT/dx is the deriative of temperature with respect to the direction of conduction, x. For plane walls, this simplifies to:

$$\dot{Q}_{cond} = -kA\frac{T_1 - T_2}{L} \tag{2.1.14}$$

where L is the distance between the two faces of the wall and T_1 and T_2 are the temperatures both surfaces.

Similar to convection, analytical results for conduction will not be carried out because of

the complex geometry. Rather, the CFD program, Star-CCM, has the capability to model conduction through a finite element formulation of the nozzle, thus yielding more accurate results. It is still useful, however, to present the basic concept of conduction here.

Computational Fluid Dynamics

CFD uses numerical methods to break fluid flow problems down into millions of small, discrete cells and resolve the flow with fluid mechanics and heat transfer equations. The solid continuum of the nozzle can also be modeled in the CFD program to determine quantities like the nozzle temperature over time and how heat conducts through the geometry.

The details of CFD will not be examined here, as it is an entire field of study in itself. A few considerations are important to note, however, in order to obtain accurate results. These will be discussed in the following paragraphs.

Prism Layers: The mesh near the surfaces needs to be long and thin, gradually increasing in thickness as the distance to the surface increases. These are known as prism layers, and the reason for this shape has to do with the boundary layer that develops near surface. In a boundary layer, the velocity changes very little parallel to the surface, but the velocity change is much greater perpendicular to the surface. This is especially true close to the surface, where the no-slip boundary condition ensures velocity is equal to zero at the surface. This boundary layer velocity gradient is shown in Fig. 5.

To capture this effectively, the distance between cells in the perpendicular direction should be small to capture the high velocity gradient, but the distance between cells can be large in the parallel direction because the velocity gradient is small. This leads to long, thin cells like those shown in Fig. 6.

Wall y+: When viewing a wall in CFD, the velocity parallel to the wall is labeled u, and the spatial coordinate perpendicular to the wall is labeled y. The boundary layer developed near the wall depends on the viscosity of the fluid and the shear stress along the wall, which

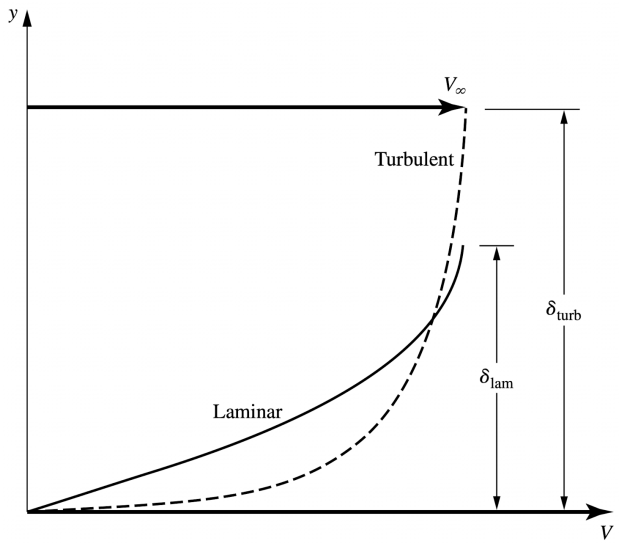

Figure 5: Boundary layer velocity profile for laminar and turbulent flows, where δ_{lam} and δ_{turb} are the boundary layer thicknesses for laminar and turbulent flow respectively [5].

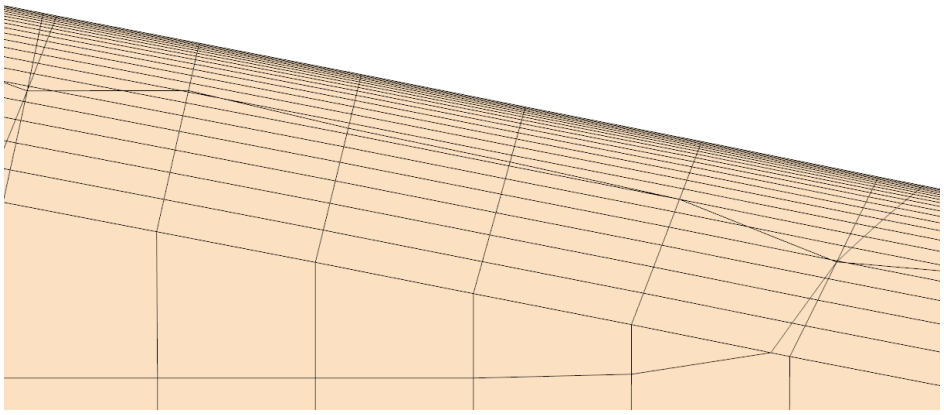

Figure 6: Prism layers are long parallel to the surface and thin perpendicular to the surface

is a function of differential velocity. Thus, for different flows and fluids, the boundary layer size will differ, and different flow scenarios will require different cell sizes near the wall to adequately capture the physics of the boundary layer. To be able to compare different flow scenarios, the position value y can be non-dimensionalized into y^+:

$$y^+ = \frac{yu_\tau}{\nu}, \quad u_\tau = \sqrt{\frac{\tau_w}{\rho}} \tag{2.1.15}$$

where u_τ is the friction or shear velocity, ν is the kinematic viscosity, τ_w is the wall shear stress, and ρ is the fluid density. Because ν is defined as μ/ρ, where μ is the dynamic

viscosity, Eq. 2.1.15 can be rewritten as [3]:

$$y^+ = \frac{y\sqrt{\tau_w \rho}}{\mu} \tag{2.1.16}$$

In addition to non-dimensionalizing y, the velocity u can also be non-dimensionalized as u^+ [3]:

$$u^+ = \frac{u}{u_\tau} \tag{2.1.17}$$

Once u and y are non-dimensionalized, a "universal" velocity profile can be plotted for *all* turbulent flows. This is shown in Fig. 7, as well as a comparison with experimental data in Fig. 8. Some important items to note are that:

- The region up to $y^+ = 5$ is laminar. Here, the velocity profile is $u^+ = y^+$.
- The buffer zone extends from $5 \leq y^+ \leq 30$. This, along with the laminar zone, comprises the boundary layer.
- The turbulent flow begins around $y^+ = 30$. Here, the velocity profile is $u^+ = C_1 log_{10}(y^+) + C_2$, where $C_1 \approx 5.6 - 5.75$ and $C_2 \approx 4.9 - 5.5$.

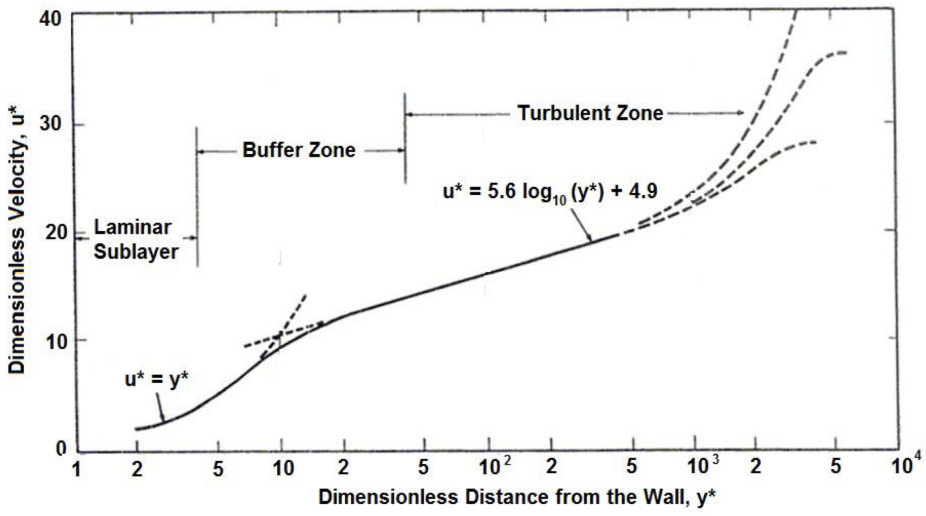

Figure 7: Universal velocity profile ($u* = u^+$, $y* = y^+$) [6]

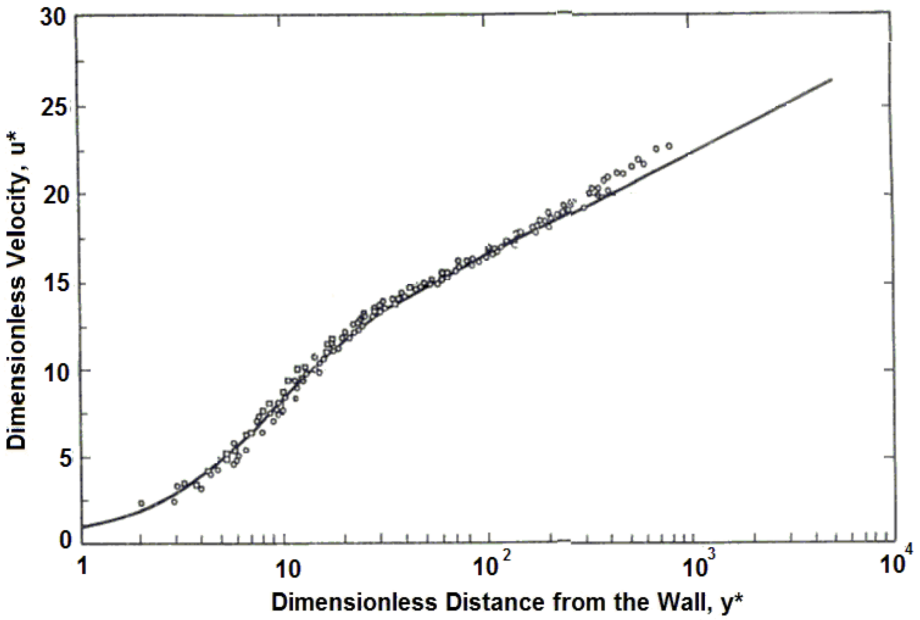

Figure 8: Universal velocity profile with experimental results overlaid [6]

This is very important in understanding whether the cells near the wall are small enough to accurately capture the velocity gradient in the boundary layer. In general, the thickness of the first cell next to a wall should satisfy $y^+ \leq 1$ to model the physics accurately. Alternatively, the wall y^+ could be set to about 30, which corresponds to the end of the buffer zone. In this case, the CFD program will model the velocity distribution in the first cell as $u^+ = y^+$. In this study, the first condition (wall $y^+ \leq 1$) will be used.

Mesh Independence: Once the model has been sufficiently refined, a *mesh independence study* can be performed to ensure the mesh sufficiently captures the physics of interest. If the mesh has an appropriate level of refinement, further refinement should not change the results. An appropriate guideline is that 20% refinement should not change results by more than 5% [4]. Once this is demonstrated, the results are said to be mesh independent.

Convergence: Convergence of a CFD simulation is typically measured by *residuals*, which correspond to the magnitude of change of a quantity from one iteration to the next. For the coupled energy and flow solvers used in this study, residuals include quantities like continuity,

energy, turbulent kinetic energy, and momentum in the x, y, and z directions. For a steady-state solution, residuals should reach very low values to indicate very little change between iterations.

Aside from solver residuals, convergence can be measured by quantities of interest that result from the simulation. In this study, this includes $\dot{m}_{out} \approx \dot{m}_{in}$ (1e−3 tolerance), a ΔP residual of 1e−3, and a $\dot{Q}_{noz}$ residual of 1e−3. Assuring that these quantities of interest have converged and are mesh independent is of utmost importance.

If residual values have "leveled out" (see Fig. 9), quantities of interest have converged, and the results remain mesh independent, the solution is considered converged.

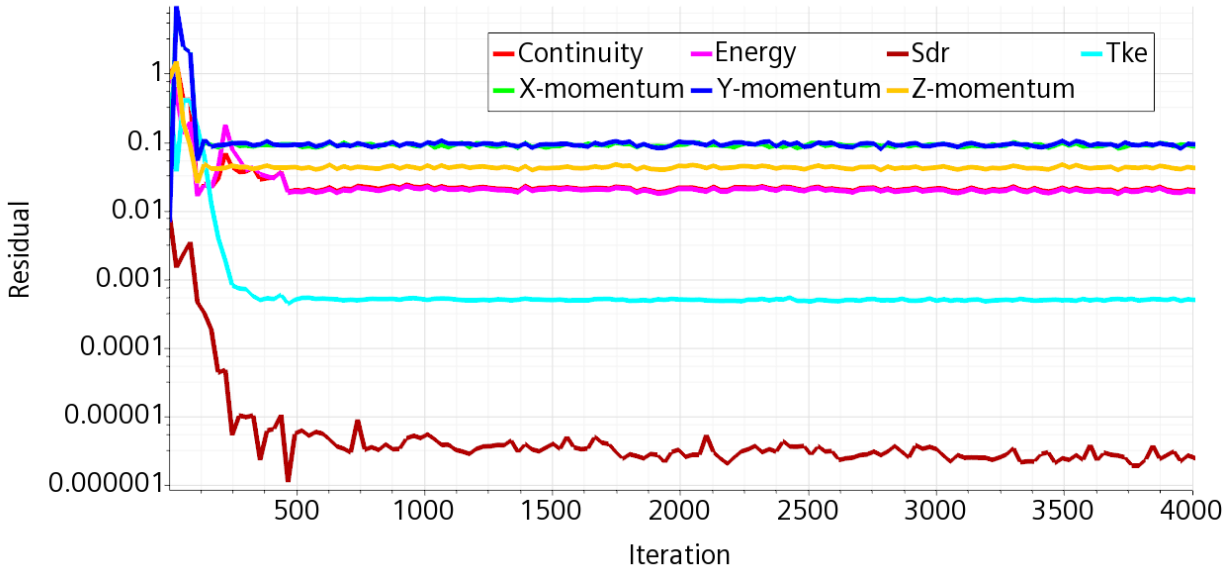

Figure 9: Residuals for 5 coil thermal nozzle for K320. Results for quantities of interest have converged and are mesh independent.

2.1.4 Heat Exchanger Model

Once heat transfer results from CFD analysis have been obtained for a certain set of conditions, a heat exchanger model can be used to find the heat transfer rate and fuel/exhaust gas outlet temperatures at off-design points, such as different throttle settings. There are two main methods of analyzing heat exchangers: the Log-Mean Temperature Distribution

(LMTD) method and the Effectiveness-NTU (ε-NTU) method. The LMTD method is useful when heat transfer requirements are known but the size of the heat exchanger needs to be identified. The ε-NTU method, on the other hand, allows one to predict the heat transfer rate and outlet temperatures for both the cold and hot fluids given a predetermined heat exchanger type and sizing. Given that the size of the thermal nozzle is determined by the size constraints of the turbojet it's used for, the ε-NTU method is better suited to find the temperature the fuel is preheated to.

Effectiveness-NTU

The first component of the ε-NTU method is heat transfer effectiveness, defined as [34]:

$$\varepsilon = \frac{\dot{Q}}{\dot{Q}_{max}} = \frac{\text{Actual heat transfer rate}}{\text{Maximum possible heat transfer rate}} \tag{2.1.18}$$

where $\dot{Q}$ is defined by a simple energy balance on the cold and hot fluids:

$$\dot{Q} = C_c(T_{c,out} - T_{c,in}) = C_h(T_{h,in} - T_{h,out}) \tag{2.1.19}$$

where $C_c = \dot{m}_c c_{pc}$ and $C_h = \dot{m}_h c_{ph}$ are the heat capacity rates of the cold and hot fluids respectively. The maximum possible heat transfer rate, $\dot{Q}_{max}$, can be determined by multiplying $C_{min} = \min(C_c, C_h)$ by the largest temperature difference between the two fluids, $\Delta T_{max} = T_{h,in} - T_{c,in}$. Substituting into Eqn. 2.1.18, this gives:

$$\varepsilon = \frac{\dot{Q}}{\dot{Q}_{max}} = \frac{C_c(T_{c,out} - T_{c,in})}{C_{min}(T_{h,in} - T_{c,in})} = \begin{cases} \frac{T_{c,out} - T_{c,in}}{T_{h,in} - T_{c,in}} & C_{min} = C_c \\ \frac{T_{h,out} - T_{h,in}}{T_{h,in} - T_{c,in}} & C_{min} = C_h \end{cases} \tag{2.1.20}$$

Relationships exist that define the effectiveness by geometry and flow arrangement. Geometries could include shell-and-tube, double pipe, or cross-flow, while flow arrangements include either parallel flow or counter flow. These relations for ε incorporate a quantity known as the number of transfer units, NTU, defined as [34]:

$$NTU = \frac{UA_s}{C_{min}} \tag{2.1.21}$$

where U is the overall heat transfer coefficient and A_s is the heat transfer surface area. Because the thermal nozzle geometry is not a standard geometry, these relations can't be used with high levels of accuracy. If the reader is curious, these can be found in Chapter 11 of [34].

If one has access to the inlet and outlet temperatures, the specific heat capacities, and the mass flow rates of both fluids, ε can be calculated and used to find the heat transfer rate and outlet temperatures given an arbitrary set of inlet temperatures. This is shown in the following Eqns.

$$\dot{Q} = \varepsilon C_{min}(T_{h,in} - T_{c,in}) \tag{2.1.22}$$

$$T_{h,out} = T_{h,in} - \frac{\dot{Q}}{\dot{m}_h c_{p,h}} \tag{2.1.23}$$

$$T_{c,out} = T_{c,in} + \frac{\dot{Q}}{\dot{m}_c c_{p,c}} \tag{2.1.24}$$

For the case of the thermal nozzle, the hot fluid is the exhaust gas, and the cold fluid is the fuel. The effectiveness can be determined numerically from CFD analysis or experimentally from temperature measurements.

2.1.5 Engine Cycle Analysis

Engine cycle analysis involves characterizing the thermodynamic changes to the working fluid (air) as it travels through the engine. This can be separated into two main categories: parametric cycle analysis (also known as *design-point* or *on-design* analysis) and engine performance analysis (also known as *off-design* analysis). Parametric cycle analysis (PCA) allows one to relate how design choices, such as the compressor pressure ratio, turbine inlet

temperature, and design point flight conditions, relate to performance characteristics, such as specific thrust or thrust specific fuel consumption. Once a particular set of design parameters has been selected, engine performance analysis (EPA) allows one to evaluate the engine performance at different flight conditions and throttle settings [21].

Parametric Cycle Analysis

Definitions: Key thermodynamic properties of the working fluid that will be studied as it passes through the engine are total temperature (T_t) and total pressure (P_t). Both of these are defined as the temperature or pressure that is reached when a moving fluid is brought to rest. Eqns. 2.1.25 and 2.1.26 show the relationship between static temperature and pressure respectively and the Mach number of the flow.

$$T_t = T\left(1 + \frac{\gamma - 1}{2}M^2\right) \tag{2.1.25}$$

$$P_t = P\left(1 + \frac{\gamma - 1}{2}M^2\right)^{\gamma/(\gamma-1)} \tag{2.1.26}$$

From these, it is evident that T_t and P_t are related by:

$$\frac{P_t}{P} = \left(\frac{T_t}{T}\right)^{\gamma/(\gamma-1)} \tag{2.1.27}$$

It is also important to define temperature and pressure ratios, which are given by:

$$\pi_a = \frac{\text{total pressure leaving component } a}{\text{total pressure entering component } a} \tag{2.1.28}$$

$$\tau_a = \frac{\text{total temperature leaving component } a}{\text{total temperature entering component } a} \tag{2.1.29}$$

The station numbers that will be used in property subscripts have been defined previously in Fig. 3.

Assumptions: The cycle analysis presented in this section assumes the flow through the engine is 1-dimensional, steady flow. The working fluid is air that is assumed to behave as a calorically perfect gas upstream of the burner (constant γ_c, $c_{p,c}$) and downstream of the burner (constant γ_t, $c_{p,t}$). Finally, the exhaust gas is assumed to be perfectly expanded at the nozzle outlet such that $P_9 = P_0$.

With these assumptions defined, the PCA process is presented in the following paragraphs.

1. Compute Free Stream Total Properties: This process involves taking static temperature and pressure of the free stream (T_0 and P_0) along with the Mach number (M_0) and combining them into the total properties T_{t0} and P_{t0}, as defined by Eqns. 2.1.25 and 2.1.26. From this, one can define the total temperature ratio of the free stream as $\tau_r = T_{t0}/T_0$, and the pressure ratio as $\pi_r = P_{t0}/P_0$.

2. Inlet: Here, the pressure ratio across the inlet is defined as $\pi_d = P_{t2}/P_{t0} = \pi_{d,max}\eta_r$, where η_r is the portion of ram total pressure recovered from the flow. The maximum pressure ratio for the inlet, $\pi_{d,max}$, is determined by its geometry, and η_r is equal to 1 for subsonic flows.

3. Compressor: In PCA, the compressor pressure ratio is a parameter determined by the designer. This is used to find the total temperature at the exit of the compressor, T_{t3}:

$$T_{t3} = T_{t2}(\pi_c)^{\frac{\gamma_c - 1}{\gamma_c e_c}} \tag{2.1.30}$$

where e_c is the *polytropic efficiency* of the compressor, which is the differential equivalent of a component's isentropic efficiency. This is typically limited by the level of technology (LOT) of the engine. An outline of typical LOT values for various component efficiencies is given by Table 2.

Table 2: Component efficiencies, total pressure ratios, and temperature limits by Level of Technology (LOT) [21].

Component	Figure of Merit	Type[a]	Level of Technology[b] 1	2	3	4	5
Diffuser	$\pi_{d,max}$	A	0.90	0.95	0.98	0.995	0.998
		B	0.88	0.93	0.96	0.98	0.985
		C	0.85	0.90	0.94	0.96	0.97
Compressor	e_c		0.80	0.84	0.88	0.90	0.91
Fan	e_f		0.78	0.82	0.86	0.89	0.92
Burner	π_b		0.90	0.92	0.94	0.95	0.96
	η_b		0.88	0.94	0.99	0.999	0.999
Turbine	e_t	Uncooled	0.80	0.85	0.89	0.90	0.91
		Cooled		0.83	0.87	0.89	0.90
Mixer	$\pi_{M,max}$			0.95	0.97	0.98	0.985
Afterburner	π_{AB}		0.90	0.92	0.94	0.95	0.96
	η_{AB}		0.85	0.91	0.96	0.99	0.995
Nozzle	π_n	D	0.95	0.97	0.98	0.995	0.997
		E	0.93	0.96	0.97	0.98	0.99
		F	0.90	0.93	0.95	0.97	0.98
Mechanical Shaft	η_m	Shaft only	0.95	0.97	0.99	0.995	0.996
		With power takeoff	0.90	0.92	0.95	0.97	0.98
Max T_{t4}		(K)	1100	1390	1780	2000	2220
		(R)	2000	2500	3200	3600	4000
Max T_{t7}		(K)	1390	1670	2000	2220	2440
		(R)	2500	3000	3600	4000	4400

[a] A = subsonic aircraft with engines in nacelles, B = subsonic aircraft with engine(s) in airframe, C = supersonic aircraft with engine(s) in airframe, D = fixed-area convergent nozzle, E = variable-area convergent nozzle, F = variable-area convergent-divergent nozzle

[b] Levels of technology (LOT) are 20-year increments starting at 1945. So, LOT 3 would represent typical component efficiency values for the time period 1985-2005.

4. Burner: Burner analysis is conducted using the first law of thermodynamics to balance the energy entering and leaving the compressor:

$$\dot{m}_f h_{PR} \eta_b + \dot{m}_0 c_{p,c} T_{t3} = (\dot{m}_0 + \dot{m}_f) c_{p,t} T_{t4} \tag{2.1.31}$$

$$f h_{PR} \eta_b + c_{p,c} T_{t3} = (1 + f) c_{p,t} T_{t4} \tag{2.1.32}$$

where $\dot{m}_f$ is the mass flow rate of the fuel, h_{PR} is the heat of combustion of the fuel, η_b is the burner efficiency, $\dot{m}_0$ is the mass flow rate of air, $c_{p,t}$ is the specific heat capacity of the air on the turbine side of the engine, $c_{p,c}$ is the specific heat capacity of air on the compressor side of the engine, and f is the fuel-to-air ratio.

Two specific heat values are used because the large temperature change from the burner causes a significant change in the specific heat capacity of the working fluid. Because $c_{p,c}$, $c_{p,t}$, and T_{t3} are all fixed, and T_{t4} is usually determined by $T_{t4,max}$, this analysis determines the fuel flow rate required to bring about these values, $\dot{m}_f$.

It is important to note that this is where h_{PR} and η_b enter the overall engine cycle analysis. Recall that these are quantities the thermal nozzle seeks to improve as a means to improve η_T and TSFC. Based on discussion in section 2.1.1, increasing the fuel temperature should increase its enthalpy, thus making the enthalpy of reactants, H_R, larger and increasing the heat of combustion, h_{PR}. From Eq. 2.1.31, this would in turn increase T_{t4}.

Additionally, as discussed in section 2.1.2, raising the fuel temperature will increase the adiabatic flame temperature, T_{ad}. While the combustor is not adiabatic, this still has the effect of increasing the energy produced by the reaction and will raise T_{t4} by some degree.

Finally, as will be discussed in section 2.2.2, increasing combustion reactant temperatures has been shown in literature to increase η_b. This will also have the effect of raising T_{t4}. To maintain the same throttle in the presence of these T_{t4}-increasing factors, $\dot{m}_f$ should be reduced. Therefore, preheating the fuel using the thermal nozzle proposed by this study should reduce fuel consumption, improving both η_T and TSFC.

5. Turbine: The goal of the turbine is to extract energy from the flow to power the compressor. Thus, a power balance is performed to find the total temperature at the turbine exit.

$$\dot{W}_{comp} = \eta_m \dot{W}_{turb} \rightarrow \dot{m}_0 c_{p,c}(T_{t3} - T_{t2}) = \eta_m(\dot{m}_0 + \dot{m}_f)c_{p,t}(T_{t4} - T_{t5}) \tag{2.1.33}$$

$$T_{t5} = T_{t4} - \frac{c_{p,c}(T_{t3} - T_{t2})}{(1+f)\eta_m c_{p,t}} \tag{2.1.34}$$

where η_m is the efficiency of the mechanical shaft at transmitting power from the turbine to the compressor. Furthermore, the pressure ratio of the turbine is determined from its polytropic efficiency, e_t:

$$\pi_t = \left(\frac{T_{t5}}{T_{t4}}\right)^{\frac{\gamma_t}{(\gamma_t - 1)e_t}} \tag{2.1.35}$$

6. Nozzle: Finally, nozzle analysis is performed to determine the exit velocity of the exhaust gas, V_9. First, the ratios of total to static pressure and temperature at the exit are found using Eqns. 2.1.36 and 2.1.37 respectively. Next, V_9 is computed from dynamic temperature $(T_{t9} - T_9)$ using Eqn. 2.1.38.

$$\frac{P_{t9}}{P_9} = \pi_r \pi_d \pi_c \pi_b \pi_t \pi_n \frac{P_0}{P_9} \tag{2.1.36}$$

$$\frac{T_{t9}}{T_9} = \left(\frac{P_{t9}}{P_9}\right)^{(\gamma_t - 1)/\gamma_t} \tag{2.1.37}$$

$$V_9 = \sqrt{(T_{t9} - T_9) 2 g_c c_{p,t}} \tag{2.1.38}$$

where π_n is the nozzle pressure ratio determined by the LOT, other pressure ratios are known, P_0/P_9 is 1 for perfect expansion, and g_c is the constant of proportionality (1 for SI units and 32.174 ft·lbm/(lbf $\cdot$ s^2) for English units).

Using this velocity and the mass flow rates, the engine thrust (F) can be determined:

$$F = \frac{(\dot{m}_0 + \dot{m}_f)V_9 - \dot{m}_0 V_0}{g_c} \tag{2.1.39}$$

7. Figures of Merit: From the engine properties determined in the previous steps, figures of merit can be determined. This includes specific thrust ($F/\dot{m}_0$), thrust specific fuel consumption (TSFC), thermal efficiency (η_T), propulsive efficiency (η_p), and overall efficiency (η_o).

$$\frac{F}{\dot{m}_0} = \frac{1}{g_c}\left[(1+f)V_9 - V_0\right] \tag{2.1.40}$$

$$\text{TSFC} = \frac{\dot{m}_f}{F} = \frac{f}{F/\dot{m}_0} \tag{2.1.41}$$

$$\eta_T = \frac{(1+f)V_9^2 - V_0^2}{2g_c f h_{PR}} \tag{2.1.42}$$

$$\eta_p = \frac{2g_c V_0 (F/\dot{m}_0)}{(1+f)V_9^2 - V_0^2} \tag{2.1.43}$$

$$\eta_o = \eta_T \eta_p = \frac{V_0}{\text{TSFC} \cdot h_{PR}} \tag{2.1.44}$$

It should be noted that for a static test stand, $V_0 = 0$, which makes η_p and η_o equal to 0. Therefore, these figures of merit will not be evaluated for the thermal nozzle. Additionally, V_9 and $\dot{m}_0$ are difficult to measure compared to $\dot{m}_f$ and F. Because of this and the fact that TSFC is the desired figure of merit to be improved, specific thrust and η_T will also not be evaluated for the thermal nozzle. This leaves TSFC as the figure of merit to be evaluated.

Summary: The theory presented in this section shows how a given set of flight conditions, component efficiencies, and design choices impacts the thermodynamic properties of the working fluid as it passes through the engine and the figures of merit that characterize the overall performance of the engine. The design choices for a turbojet are the compressor pressure ratio (π_c) and the turbine inlet temperature (T_{t4}). The former is limited by

geometric constraints for the compressor, while the latter is limited by the material of the turbine.

Engine Performance Analysis

Once PCA has been completed and engine design parameters have been selected, engine performance analysis (EPA) is performed to evaluate the engine's behavior at different flight conditions and throttle settings. In this study, the engine will only be run on a static test stand where throttle setting is varied.

Assumptions: The following assumptions are made when carrying out EPA [21]:

- The flow is choked at the entrance nozzles to the high and low pressure turbines and at the primary exit nozzle.
- The pressure ratios of the main burner and primary exit nozzle (π_b and π_n) remain constant.
- All component efficiencies remain constant.
- Turbine cooling and leakage effects are neglected.
- Power is not removed from the turbine to drive accessories.
- Gases are calorically perfect both upstream and downstream of the main burner.
- γ_t, c_{pt}, and R_t do not vary with the throttle setting (T_{t4}).
- The term $(1 + f)$ is considered constant, since $\dot{m}_0 \gg \dot{m}_f$.
- The gas at the nozzle exit is perfectly expanded ($P_9 = P_0$).

With these assumptions defined, the EPA process is presented in the following paragraphs.

1. Compute Free Stream Total Properties: Like in PCA, the first step is to compute the free stream total properties from the static properties and Mach number. This is done using Eqs. 2.1.25 and 2.1.36.

2. Inlet: This step is also the same as for PCA, where the ratio across the inlet is obtained by $\pi_d = P_{t2}/P_{t0} = \pi_{d,max}\eta_r$.

3. Turbine: Because of the assumptions of choked flow at the turbine entrance, constant turbine efficiency η_T, and constant values for γ_t, c_{pt}, and R_t, the π_t and τ_t obtained from PCA remain constant in EPA. Based on the throttle setting (T_{t4}) for which EPA is being performed, T_{t5} can be obtained simply by $T_{t5} = \tau_t T_{t4}$.

4. Compressor: Now that T_{t4} and T_{t5} are both known, a power balance can be applied to the turbine and compressor, where η_m is the efficiency of the mechanical shaft at transmitting power:

$$\begin{aligned} & \dot{W}_c = \eta_m \dot{W}_t \\ \rightarrow \quad & \dot{m}_0 c_{pc}(T_{t3} - T_{t2}) = \eta_m(\dot{m}_0 + \dot{m}_f)c_{pt}(T_{t4} - T_{t5}) \\ \rightarrow \quad & c_{pc}(T_{t3} - T_{t2}) = \eta_m(1+f)c_{pt}(T_{t4} - T_{t5}) \end{aligned} \tag{2.1.45}$$

This allows one to obtain T_{t3}:

$$T_{t3} = \frac{\eta_m(1+f)c_{pt}(T_{t4} - T_{t5})}{c_{pc}} + T_{t2} \tag{2.1.46}$$

which can then be used to find π_c:

$$\pi_c = \left(\frac{T_{t3}}{T_{t2}}\right)^{\gamma_c e_c/(\gamma_c - 1)} \tag{2.1.47}$$

Now that π_c is known, the mass flow rate of air can be found using a mass flow parameter relation that simplifies to [22]:

$$\dot{m}_0 = \dot{m}_{0R} \frac{P_0 \pi_r \pi_d \pi_c}{(P_0 \pi_r \pi_d \pi_c)_R} \sqrt{\frac{T_{t4R}}{T_{t4}}} \tag{2.1.48}$$

where the quantities with the R subscript are reference quantities obtained from PCA. The updated mass flow rate will be used later to calculate thrust.

5. Burner: Since T_{t3} is now known, an energy balance can be applied to the main burner:

$$\eta_b \dot{m}_f h_{PR} = (\dot{m}_0 + \dot{m}_f) c_{pt} T_{t4} - \dot{m}_0 c_{pc} T_{t3} \tag{2.1.49}$$

which can be rearranged to find the fuel mass flow rate, $\dot{m}_f$:

$$\dot{m}_f = \frac{\dot{m}_0 (c_{pt} T_{t4} - c_{pc} T_{t3})}{\eta_b h_{PR} - c_{pt} T_{t4}} \tag{2.1.50}$$

The fuel-to-air ratio, f, can be found simply by dividing both sides by $\dot{m}_0$. Similar to the discussion for the burner in PCA, it is clear here that increasing either η_b or h_{PR} will reduce f, which has the effect of improving η_T and TSFC.

6. Nozzle: Assuming there is no afterburner, T_{t9} can be taken to equal T_{t5}. To find the static temperature T_9 at the nozzle exit, P_{t9}/P_9 must first be found:

$$\frac{P_{t9}}{P_9} = \pi_r \pi_d \pi_c \pi_b \pi_t \pi_n \left(\frac{P_9}{P_0} \right) \tag{2.1.51}$$

where $P_9/P_0 = 1$ because of the perfect expansion assumption. Next, T_9 is found:

$$\frac{T_{t9}}{T_9} = \left(\frac{P_{t9}}{P_9} \right)^{(\gamma_t - 1)/\gamma_t} \quad \rightarrow \quad T_9 = \frac{T_{t9}}{(P_{t9}/P_9)^{(\gamma_t - 1)/\gamma_t}} \tag{2.1.52}$$

Finally, V_9 can be found from the difference in total and static temperatures at station 9:

$$V_9 = \sqrt{(T_{t9} - T_9) 2 g_c c_{pt}} \tag{2.1.53}$$

Since the new mass flow rates for air and fuel have been determined, these can be used with V_9 to calculate the thrust using Eq. 2.1.39.

7. Figures of Merit: The equations for figures of merit – which includes $F/\dot{m}_0$, TSFC, η_T, η_p, and η_o – are the same for EPA as in PCA (Eqs. 2.1.40 - 2.1.44). As stated before, a static test stand will make $V_0 = 0$, and thus $\eta_p = \eta_o = 0$.

Summary: This section has shown how an engine that has been designed for a certain throttle setting and flight condition can be evaluated at different throttle settings. While the assumptions made will reduce the accuracy of the analysis by some degree, they are reasonable assumptions that will still yield good preliminary performance results for the engine [21].

Comparing EPA and Experimental Results

The performance characteristics determined by EPA correspond to the given flight condition (T, P, and M) and throttle setting (T_{t4}). Experimental measurements can be gathered from many combinations of these properties, and in order to compare results, the resultant properties must be corrected to a common reference datum. This is commonly chosen to be sea-level static conditions: $T_{ref} = 518.69°\text{R}$ (288.2 K) and $P_{ref} = 14.696$ psia (101,300 Pa).

EPA for this study is performed at sea-level static conditions, so no corrections to these results are necessary. Experimental results, however, need to be corrected to compare with EPA and with one another. Since TSFC is the quantity of interest for this study, F and $\dot{m}_f$ are the experimental quantities that need to be corrected. To do this, total pressure and temperature are non-dimensionalized with respect to the reference conditions:

$$\delta_i = \frac{P_{ti}}{P_{ref}} \tag{2.1.54}$$

$$\theta_i = \frac{T_{ti}}{T_{ref}} \tag{2.1.55}$$

From here, the corrected thrust and fuel flow rate are given by:

$$F_c = \frac{F}{\delta_0} \tag{2.1.56}$$

$$\dot{m}_{fc} = \frac{\dot{m}_f}{\delta_2\sqrt{\theta_2}} \tag{2.1.57}$$

2.1.6 Engine Cycle Analysis with Fuel Preheating

As discussed in section 2.1.1, the heat of combustion (h_{PR}) is defined as the enthalpy of the reactants at their initial temperature minus the enthalpy of the products after they have been cooled to that same temperature. Preheating the fuel would change the initial temperature and the enthalpy of the reactants, thereby changing h_{PR}.

Adding Fuel Heating to Parametric Cycle Analysis

The rate of heat being added to the fuel ($\dot{Q}_{f,noz}$), and consequently being added to the flow of the engine, can be included in Eq. 2.1.31 by adding the $\dot{Q}_{f,noz}$ term:

$$\dot{Q}_{f,noz} + \dot{m}_f h_{PR}\eta_b = (\dot{m}_0 + \dot{m}_f)c_{p,t}T_{t4} - \dot{m}_0 c_{p,c}T_{t3} \tag{2.1.58}$$

Adding $\dot{Q}_{f,noz}$ to the energy balance will necessarily increase T_{t4}. Additionally, the increased fuel temperature $T_{f,out}$ will change h_{PR} as described by the EES method in section 2.1.1, further affecting T_{t4}. To achieve the desired T_{t4}, $\dot{m}_f$ should be adjusted accordingly. Because $\dot{m}_f$ impacts the amount of heat transfer in the nozzle, as shown by the relationships in section 2.1.4, updating $\dot{m}_f$ will change $\dot{Q}_{f,noz}$ and $T_{f,out}$, necessitating another iteration of the cycle analysis. This process is repeated until the updated $\dot{m}_f$ does not produce a change in $\dot{Q}_{f,noz}$ or h_{PR}. Once the system stabilizes, the ε-NTU model can be used to find the new

exhaust gas outlet temperature, T_{t9}. This iterative process is outlined in Fig. 10.

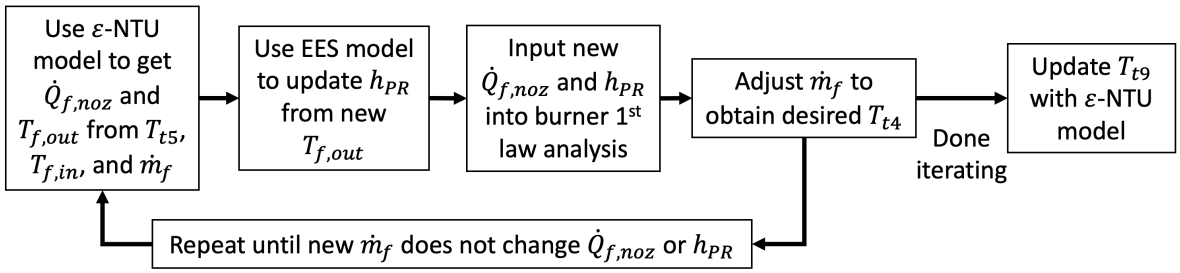

Figure 10: The process to add $\dot{Q}_{f,noz}$ and updated h_{PR} to PCA

Adding Fuel Heating to Engine Performance Analysis

Adding the fuel heating from the nozzle, $\dot{Q}_{f,noz}$, to EPA is a very similar process to adding it to PCA. The main difference is that instead of adjusting $\dot{m}_f$ manually to obtain a desired T_{t4}, $\dot{m}_f$ is calculated as part of the EPA procedure. The process shown in Fig. 10 becomes the process shown in Fig. 11.

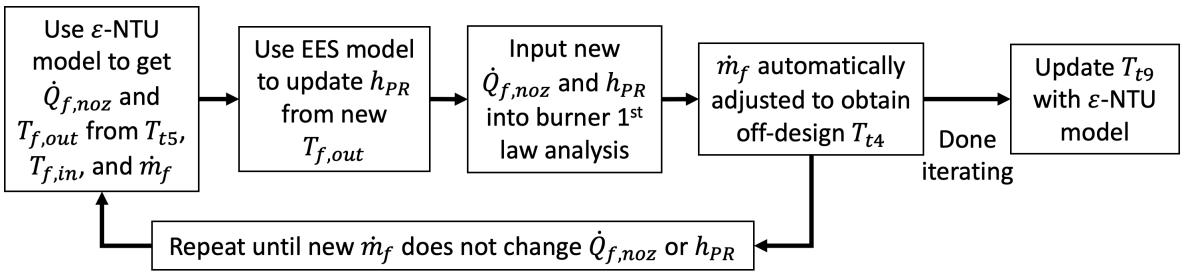

Figure 11: The process to add $\dot{Q}_{f,noz}$ and updated h_{PR} to EPA

2.2 Review of Literature

2.2.1 Thermal Efficiency & TSFC

Recall that decreased thermal efficiency leads to increased TSFC, and thermal efficiency is highly dependent on π_c (Eqns. 2.1.2 and 2.1.1). Because small-scale turbine engines are limited by their smaller geometries, π_c values are typically much lower than those of their large-scale counterparts, leading to higher TSFC. This is shown clearly in Fig. 12, where

large-scale turbine engines generally have higher π_c and lower TSFC. One caveat to this figure, as noted in the caption, is that the large-scale engines are turbofans, not turbojets. This is because modern large-scale engines are almost always turbofans for efficiency reasons. To make results comparable, low-bypass turbofans (BPR ≤ 0.76) are chosen for the large-scale examples to minimize the effect of air bypass on TSFC.

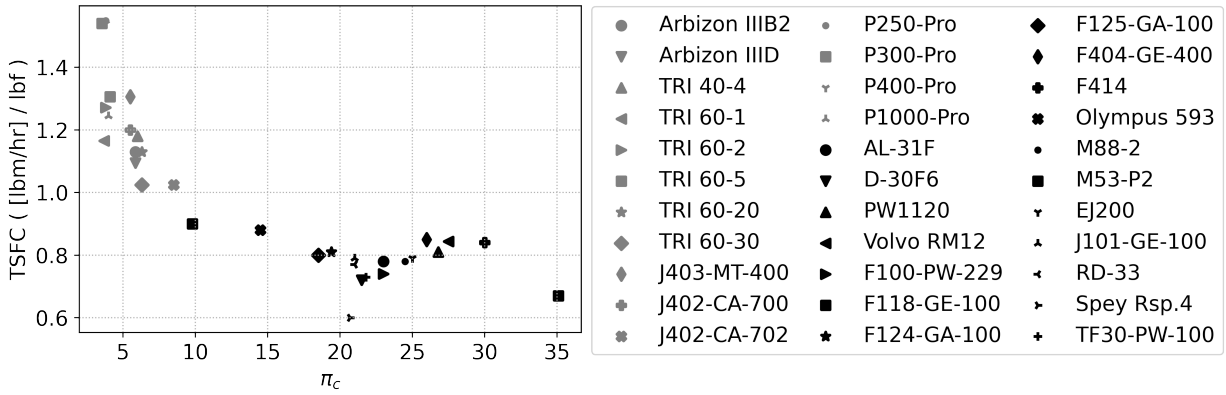

Figure 12: TSFC vs. compressor pressure ratio for small-scale (gray) and large-scale (black) gas turbine engines [26, 8, 21, 16, 14, 17, 15]. An important note is that most of the large scale engines are low-bypass turbofans (BPR ≤ 0.76), whereas the small-scale engines are all turbojets.

As discussed in section 2.1, an alternative to increasing π_c as a means to improve TSFC is to recuperate heat from the exhaust gas to preheat the fuel before it enters the engine.

2.2.2 Previous Studies on Preheating Combustion Reactants

While small-scale turbine engines don't typically preheat fuel before it enters the combustor, modern large-scale aircraft preheat the fuel as much as possible. One benefit is that heating the fuel prevents ice crystals from forming in the fuel lines at high altitudes and cold climates [2]. Another benefit, as already mentioned, is that preheating the fuel improves engine efficiency. More importantly in large-scale applications, though, is that fuel is used to cool hot engine components as cycle temperatures are pushed higher and higher in modern turbine engines [11]. Heating is achieved through devices such as Fuel-Cooled Oil Coolers (FCOCs) and routing fuel around hot components. Additionally, fuel is *cooled* through devices like ram

air heat exchangers and wing cooling to increase its thermal capacity for further component cooling, as well as to regulate the fuel temperature to avoid thermal instability that leads to coking and fuel nozzle clogging. This cycle is demonstrated in Fig. 13.

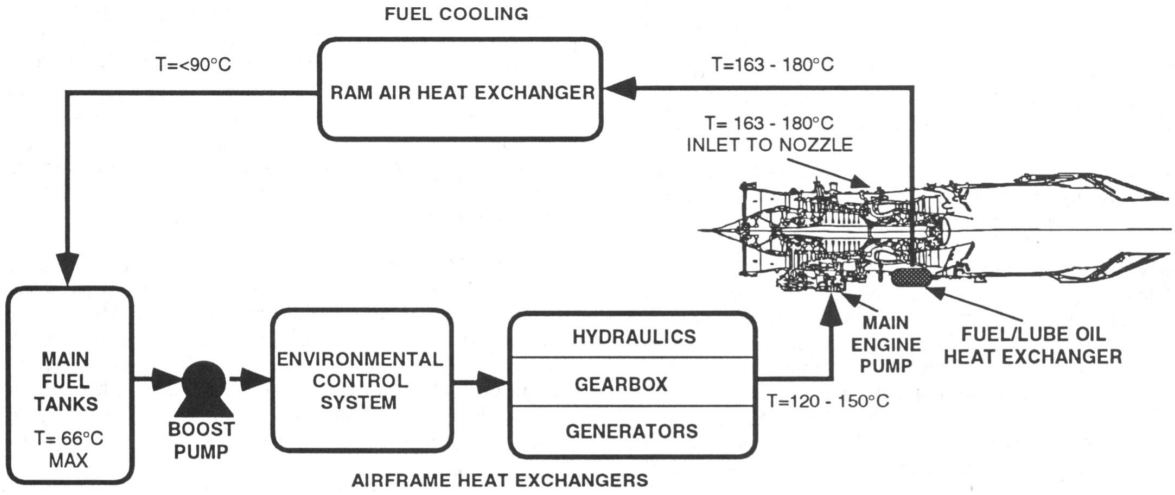

Figure 13: Fuel heating / cooling cycle on advanced fighter aircraft [11]

Effect of Preheat on Adiabatic Flame Temperature

The impact of fuel preheat on adiabatic flame temperature, T_{ad} has generally been found to be less significant than that of air preheat. One study by Tourlidakis and Malkogianni performed a combustion analysis that includes dissociation effects in calculating the final, adiabatic flame temperature of the products. This was done for both a low calorific value (LCV) fuel and a high calorific value (HCV) fuel. As can be seen from the results, increasing inlet air temperature incrementally (Fig. 14) has a much greater effect on T_{ad} than increasing inlet fuel temperature by corresponding increments (Fig. 15).

Effect of Preheat on Burner & Overall Efficiency

Several studies have been found in literature that investigate the effect of fuel preheating on gas turbine performance. One study analyzed this for power generation gas turbines for several fuel types: natural gas, syngas, and aviation kerosene [20]. In all cases, turbine efficiency increased, although the effect was higher for natural gas than aviation kerosene.

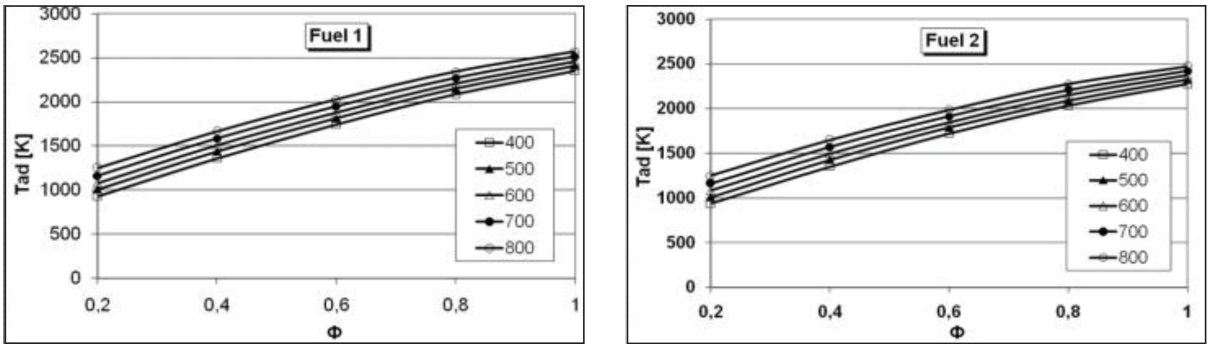

(a) HCV fuel (b) LCV fuel

Figure 14: Mathematical results for air preheat at various temperatures [29]

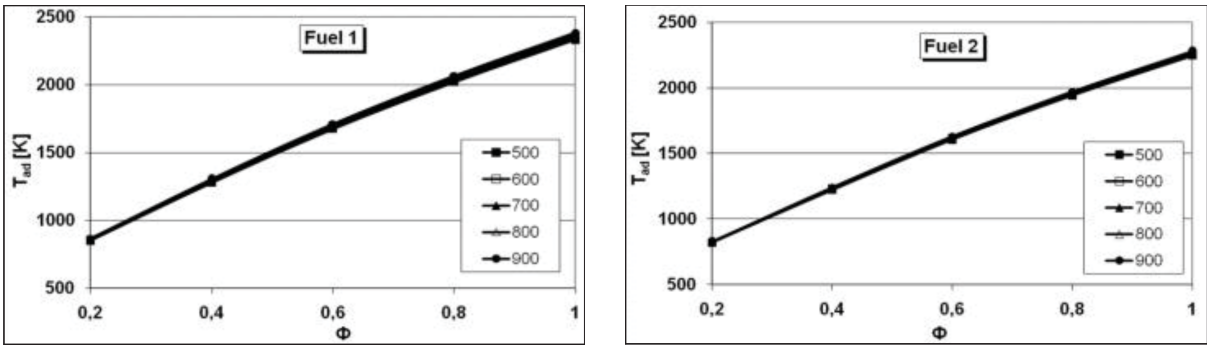

(a) HCV fuel (b) LCV fuel

Figure 15: Mathematical results for fuel preheat at various temperatures [29]

Another study evaluated this effect using Jet-A in a Rolls-Royce 501K combustor with a modified fuel injector for handling two-phase flow [32]. The results show that the added enthalpy from preheating increased burner efficiency when combustion pressure was higher than the vapor pressure of Jet-A. However, when combustion pressure was lower than the vapor pressure of Jet-A, burner efficiency decreased, presumably because of changes in spray atomization and mixing.

The details of fuel temperature on burner efficiency can become quite complex, as it potentially changes the flame kinetics within the combustor. Glassman noted that for premixed combustion, the initial temperature of the reactants affects the rate of reaction, flame propagation rate, and final flame temperature [10]. Because of these changes, it is possible that achieving optimal burner efficiency in the presence of a thermal nozzle will involve modifications to the combustor. While such a task is out of scope for this study, it could

present an interesting study for the future.

Another study investigated the effect of using hot exhaust gas from a turbine to preheat both air and fuel entering the combustion chamber, similar to what is being investigated in the present study [18]. It was found that preheating air alone increased the overall cycle efficiency by about 4%, but preheating both air and fuel increased cycle efficiency by about 4.5%.

2.2.3 Thermal Stability of Fuel and Preheating Limitations

In the early 1990s, fighter aircraft were putting increasing demands on system components, and fuel was the coolant of choice to meet these thermal management concerns. However, systems designers ran into a limit on how much heat that could be dumped into the fuel. If fuel is heated above 785 R, it becomes thermally unstable, leading to fuel deposition on surfaces (also known as fuel coking). This caused unscheduled maintenance burdens that could be quite expensive. Consequently, the U.S. Air Force put effort into developing an additive that would increase the thermal stability of JP-8 fuel at high temperatures. The result was JP-8+100, an inexpensive additive that increases the thermal stability of the fuel by 100°F[11, 12, 13].

Because of these limitations, it is *critical* in designing a thermal nozzle that the fuel is not excessively preheated. If it is heated above 785 R for conventional fuels, the already poor MTBO of small-scale turbojets would only be made worse from fuel coking in components like fuel inlet nozzles.

2.3 Objectives

This study will be conducted in two stages:

1. Design of a thermal nozzle for a KingTech K320

2. Experimental and numerical evaluation of the thermal nozzle design

2.3.1 Thermal Nozzle Design Objectives

The first step is to design a thermal nozzle that meets the requirements of preheating the fuel while remaining below the fuel coking temperature of 785 R. Several design concepts will be examined, where CFD analysis will reveal heat transfer properties of the geometry as well as pressure drop through the fuel flow channels. Preliminary pressure drop experiments will also be performed on plastic 3D prints of promising candidates to assess manufacturability and validation of CFD results. The best design will be selected that minimizes pressure loss and meets the temperature criteria.

2.3.2 Experimental and Numerical Evaluation Objectives

Once a thermal nozzle design has been chosen, it will be printed in Haynes 282. Next, the test matrix as outlined in Table 3 will be performed. Ideally, results should show a decrease in TSFC for every throttle setting. All throttle settings and fuel choices will first be tested with the original nozzle mounted to validate EPA predictions. Once these have been obtained, the same tests will be performed with the thermal nozzle mounted, first without fuel running through it (baseline), then with fuel running through it. From there, the results will be compared and analyzed.

Table 3: Test Matrix for Experimental Evaluation – Will be run for both Jet A and Diesel

	Throttle %	Original Thermal (baseline) Thermal
F (lb)	20%	
	40%	
	60%	
	80%	
	100%	
$\dot{m}_f$ (lb/s)	20%	
	40%	
	60%	
	80%	
	100%	
TSFC (1/hr)	20%	
	40%	
	60%	
	80%	
	100%	
$T_{f,out}$ (R)	20%	-
	40%	-
	60%	-
	80%	-
	100%	-

CHAPTER III

METHODOLOGY

3.1 Turbojet Selection

Among the engines available in the researcher's lab, a 300N (∼70 lbf) engine was chosen for this study for several reasons. Compared with other engines in the lab, a 300N engine is relatively large. This eases the manufacturing and handling of the nozzle by avoiding small geometries and material thicknesses that could be difficult to work with. Additionally, experimental measurements like fuel flow rate and thrust will be larger in magnitude, increasing the likelihood that relatively small changes in performance results will be detected by the measurement devices.

While initial analysis was done for a JetCat P300, the KingTech K320 was used in the end because of its availability. The two engines are very similar in size and thrust output, and preliminary CFD and cycle analysis translated quite well to the final engine. Key output parameters remained roughly the same, so no design changes were necessary for the final nozzle design.

3.2 Preliminary Nozzle Designs

The starting point for the thermal nozzle was a nozzle designed by a team of Oklahoma State University students [9], shown in Fig. 16. Originally designed to improve the thrust-to-weight ratio of the JetCat P100-RX, it was scaled up for the JetCat P300 using the mass flow parameter relationship in Eqs. 3.2.1-3.2.2, where $M = 0.895$ is the optimal exit Mach number as determined by GASTAB [21]. This was subsequently scaled for the K320 by

scaling the P300 geometry to match the K320's mounting holes.

$$A_9 = \frac{(\dot{m}_0 + \dot{m}_f)(\sqrt{T_{t0}}/P_{t0})}{MFP(M = 0.895, \gamma = \gamma_t)} \tag{3.2.1}$$

$$MFP = \sqrt{\frac{\gamma g_c}{R}} M \left(1 + \frac{\gamma - 1}{2} M^2\right)^{-\frac{\gamma+1}{2(\gamma-1)}} \tag{3.2.2}$$

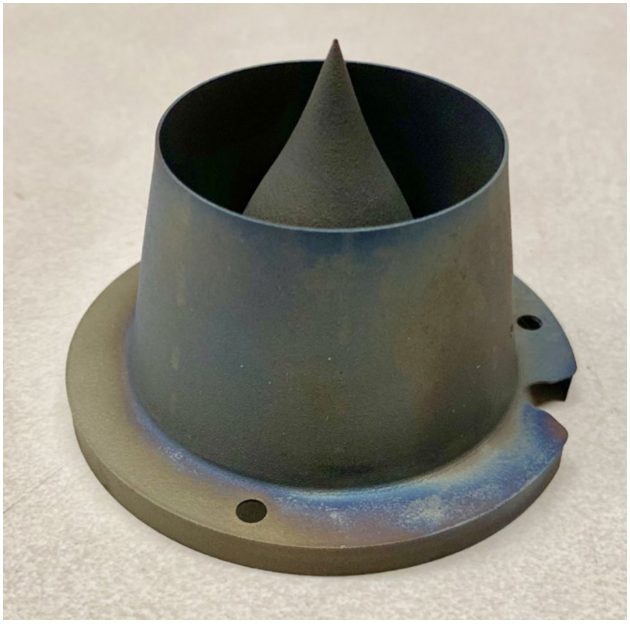

Figure 16: P100-RX nozzle designed by Oklahoma State University students [9]

The nozzle selection process started with brainstorming for a few preliminary design ideas and potential variations that could be made to those. The scaled nozzle geometry is shown in Fig. 17, where available heat exchanger volume is outside the nozzle, inside the vanes, and inside the nose cone.

Coiled: One design idea is to run the fuel through coils around the outside of the nozzle, as shown in Fig. 18. The number of coils could be varied to shorten or lengthen the path the fuel has to travel from inlet to outlet as well as vary the flow velocity.

A cross-sectional view of one of the coiled channels is shown in Fig. 19, where the width and thickness of the channel are given by w and t respectively. Since an increase in the Reynolds number generally corresponds to an increase in the convective heat transfer

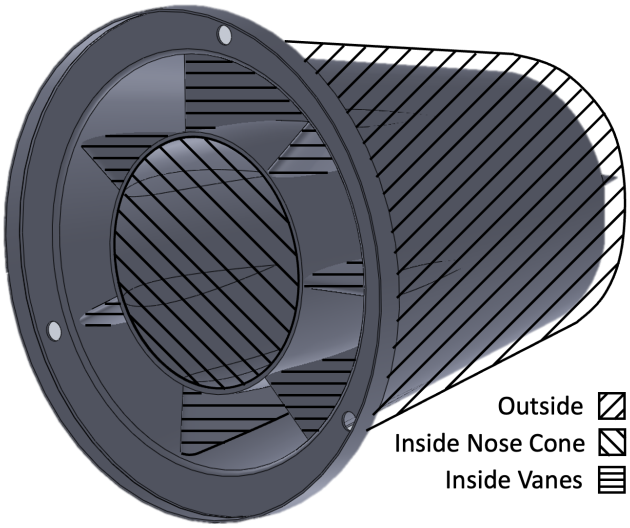

Figure 17: Scaled nozzle geometry with available heat exchanger regions shown.

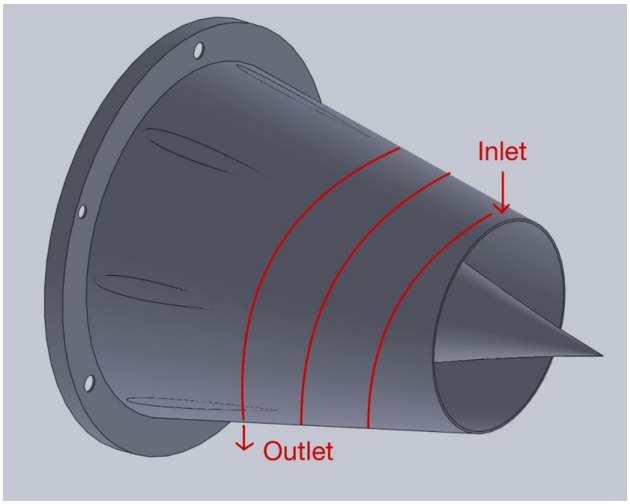

Figure 18: Coiled Heat Exchanger Sketch

coefficient, as discussed in Section 2.1.3, simple analysis of this quantity can show the effect of changing channel dimensions on the heat transfer.

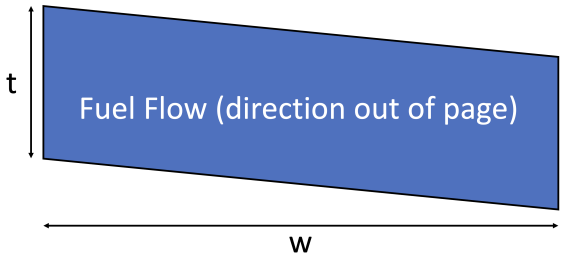

Figure 19: Cross-sectional sketch of a channel on the coiled heat exchanger

The Reynolds number definition is given by:

$$Re = \frac{\rho v D_h}{\mu} \tag{3.2.3}$$

where ρ is the fluid density, v is the flow velocity, D_h is the hydraulic diameter, and μ is the dynamic viscosity of the fluid. The flow velocity can be written in terms of mass flow rate, density, and channel dimensions:

$$\dot{m} = \rho w t v \rightarrow v = \frac{\dot{m}}{\rho w t} \tag{3.2.4}$$

and the hydraulic diameter can be written in terms of channel dimensions:

$$D_h = \frac{4A_c}{p} = \frac{4wt}{2(w+t)} = \frac{2wt}{w+t} \tag{3.2.5}$$

Substituting Eqns. 3.2.4 and 3.2.5 into Eq. 3.2.3 yields an equation that clearly demonstrates the relationship between channel dimensions and the Reynolds number:

$$Re = \frac{\rho}{\mu}\left(\frac{\dot{m}}{\rho w t}\right)\left(\frac{2wt}{w+t}\right) = \frac{2\dot{m}}{\mu(w+t)} \tag{3.2.6}$$

Increasing the number of channels while keeping the overall width of the channels constant reduces the individual channel width w. Assuming that mass flow rate remains constant, reducing w increases the Reynolds number, as seen in Eq. 3.2.6, which causes a higher convective heat transfer coefficient and higher heat transfer rate. Similarly, reducing the channel thickness, t, should also increase the heat transfer rate.

Straight Channel: Another design idea is to run the fuel through a number of straight channels along the outside of the nozzle in the axial direction, as shown in Fig. 20. This essentially adds a sleeve to the outside of the nozzle with fins in the axial direction. Increasing the number of fins would provide more heat transfer area and, theoretically, increase the heat

transfer rate.

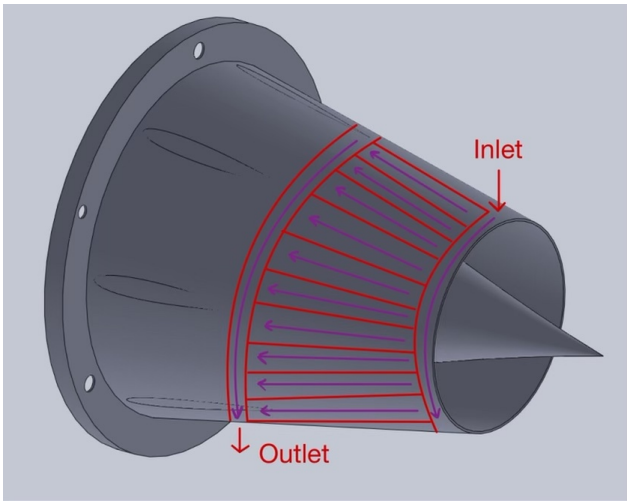

Figure 20: Straight Channel Heat Exchanger Sketch

Coiled and Internal: Another design idea is to combine the coiled heat exchanger with additional channels inside the vanes and nose cone. This would maximize the available surface area for heat transfer but would increase the overall pressure drop across the thermal nozzle. Given the temperature limit of 785 R (see Section 2.2.3), it is possible that this design would heat the fuel *too much* and cause issues with coking and thermal stability of the fuel.

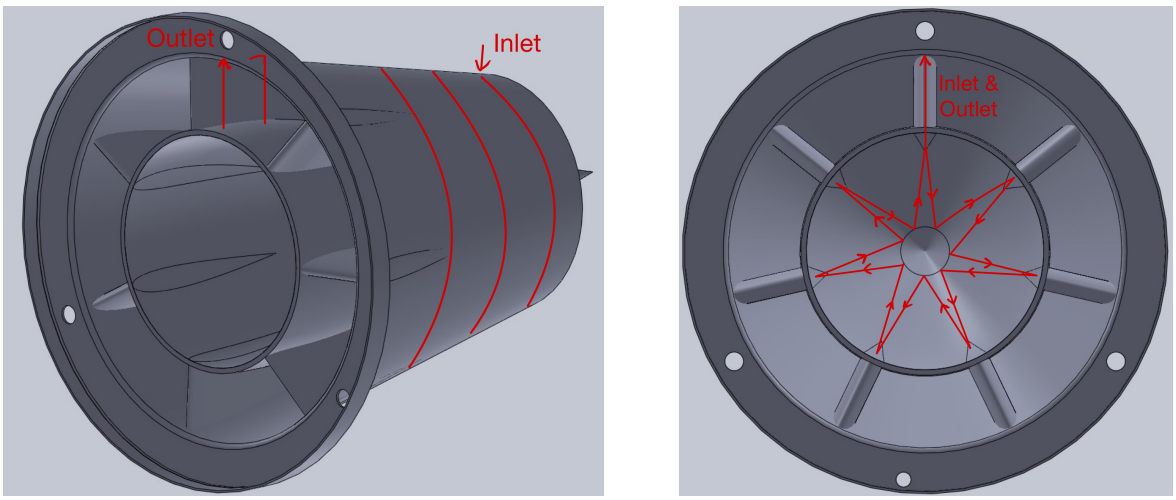

(a) Outer view (b) Inner view

Figure 21: Coiled + Inner Heat Exchanger Sketch

3.2.1 Evaluation Parameters

For each design idea and iteration, the overall effectiveness of the design will be evaluated using certain key metrics: manufacturability, heat transfer rate, fuel outlet temperature, and pressure drop. Several parameters will be varied on each design idea (Table 4) to evaluate how these impact the key metrics. The overall best design should provide the maximum heat transfer without exceeding 785 R, be easily manufacturable with 3D printing technologies, and have a low pressure drop (< 2 psi).

Table 4: Parameters to vary for the 3 design ideas

	Coiled	Straight	Coiled & Internal
Parameters to vary:	Number of coils	Number of channels (fins)	Same as Coiled
	Channel thickness	Channel thickness	Number of vanes to enter
	Overall channel width	Overall channel width	Internal channel geometry (thickness, pattern)

Design iterations will be evaluated both numerically and experimentally. Numerical analysis is conducted using CFD studies to obtain data on heat transfer rate and pressure drop. Experimental analysis is performed using a PLA 3D printer and a fixed pressure head to move water through the nozzle. Pressure drop can be measured from the mass flow rates with and without the nozzle, and these experimental results should match the CFD results.

3.2.2 CFD Evaluation

CFD evaluation was divided into two phases. In the initial phase, only the air and fuel flow domains were modeled with a simple contact interface between them for heat transfer. This allowed for multiple candidates to be examined quickly, varying parameters like the fuel flow channel thickness and number of coils. Once some promising candidates were identified, the secondary phase added the nozzle to the model to increase fidelity.

Setup

The CFD studies were performed using Star-CCM following the considerations and recommendations outlined in Section 2.1.3. Properties for the physics continua used in the simulations are given in Table 5, and the boundary conditions are shown in Table 6. The interfaces between the fluid domains and the solid nozzle domain have a Conjugate Heat Transfer thermal specification with zero contact resistance to facilitate heat transfer between the domains. The domains geometries are shown in Fig. 22, and a mesh of the air flow domain is shown in Fig. 23.

Table 5: Star-CCM physics continua properties for domains in CFD simulations

	Air Flow Domain	Fuel Flow Domain	Nozzle Domain*
Steady	x	x	x
Gas	x		
Liquid		x	
Solid			x
Gravity		x	
Three Dimensional	x	x	x
Coupled Flow	x	x	
Coupled Energy	x	x	
Coupled Solid Energy			x
Constant Density		x	
Gradients	x	x	x
Ideal Gas	x		
Turbulent	x	x	
Reynolds-Averaged Navier-Stokes	x	x	
K-Omega Turbulence	x	x	
SST (Menter) K-Omega	x	x	
Wall Distance	x	x	
All y+ Wall Treatment	x	x	
Cell Quality Remediation	x	x	
Solution Interpolation	x	x	

* This column only applicable for secondary phase of CFD evaluation.

Numerical Verification Mesh independence studies were performed on the most promising CFD results. The greatest percentage change was found in the pressure drop, but this

Table 6: Boundary conditions for CFD simulations

	Air Flow Domain			Fuel Flow Domain		
	Inlet	Outlet	Walls	Inlet	Outlet	Walls
Type	Mass Flow Inlet	Pressure Outlet	Wall	Mass Flow Inlet	Pressure Outlet	Wall
$\dot{m}$ (kg/s)	0.5	-	-	0.01323[a]	-	-
Total Temp. (R)	1914.142[b]	-	-	540	-	-
Gauge Pressure (psi)	-	0	-	-	0	-
Shear Stress Spec.	-	-	No-Slip	-	-	No-Slip
Wall Surface Spec.	-	-	Smooth	-	-	Smooth

[a] Value is for P300 simulations. The equivalent K320 value is 0.0145 kg/s.
[b] Value is for P300 simulations. The equivalent K320 value is 2047.373 R.

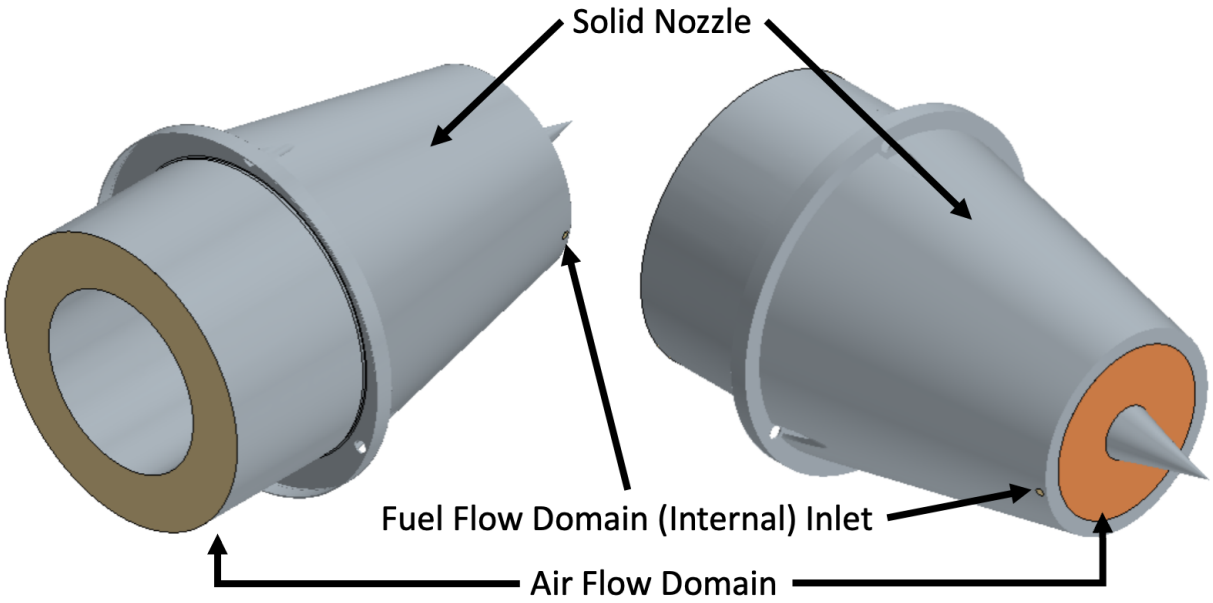

Figure 22: CFD domain geometries for secondary phase

remained below 5%, indicating an acceptable mesh independence [4]. Additionally, the wall y+ values remained near 1 or below for all simulations, indicating the prism layer mesh was sufficiently refined to resolve the boundary layer physics.

CFD Evaluation Results

Results for the initial CFD evaluation of the coiled design are shown in Table 8, where the best results are obtained from the 7 coil design with a channel thickness of 0.1in. As predicted analytically, reducing the channel thickness increases the heat transfer rate and

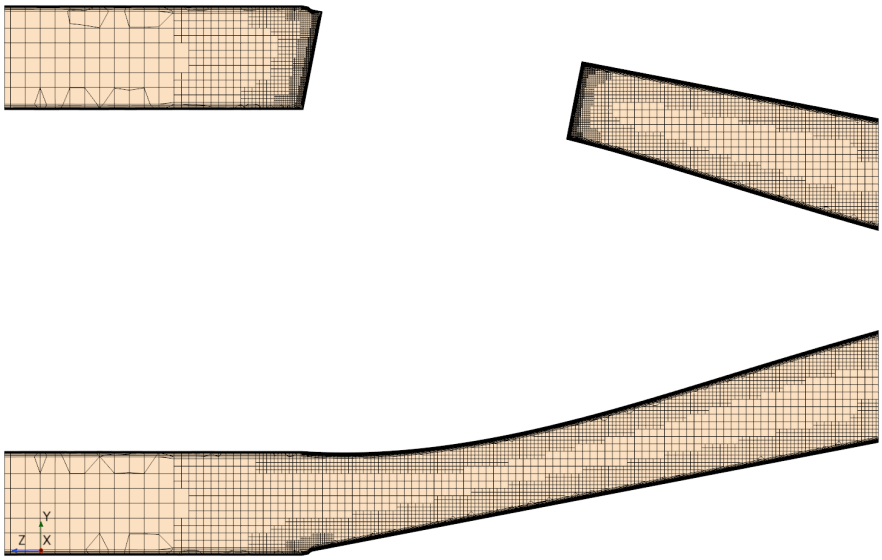

Figure 23: Axial section view of air flow domain. Note the gap where one of the vanes resides.

Table 7: CFD mesh independence study results for 5 & 7 coils, 0.1in channel thickness, rev2 design iterations.

	Mesh Refinement	Heat Transfer Rate (kW)	% diff.	Fuel Outlet Temperature (R)	% diff.	Pressure Drop (psi)	% diff.
5 Coil	Base	4.812	0.000%	765.1	0.000%	1.497	0.000%
	60%	4.78	-0.665%	759.26	-0.763%	1.44	-3.808%
7 Coil	Base	5.01	0.000%	797.1	0.000%	1.42	0.000%
	60%	5.017	0.140%	785	-1.518%	1.481	4.296%

fuel outlet temperature. However, once the channel thickness is small enough – 0.05in for these results – the pressure drop becomes unacceptably high (up to 11 psi for the 10 coil case).

After initial CFD was performed, an issue was recognized where the fuel was pooling near the inlets and outlets of the nozzle, causing excessive heating of fuel in those regions. This was corrected in the secondary phase of CFD evaluation, where results are shown in Table 9. It is shown that making this correction and adding the nozzle domain to the simulation causes the outlet temperature of the best 7 coil design to rise above the maximum limit of

Table 8: CFD initial study results for varying number of coils, channel thickness, and total channel width (reflected by surface area).

	Channel Thickness (in)	No. Cells	Surface Area*(in^2)	Heat Transfer Rate (kW)	Fuel Outlet Temperature (R)	Pressure Drop (psi)
2 Coil	0.05	13,552,686	31.198	3.1863	678.45	2.2744
	0.1	13,558,636	28.251	2.4658	653.6	1.116
	0.1	12,894,116	22.721	2.17615	640.75	1.0196
	0.15	13,787,707	25.382	2.1318	645.264	0.9402
	0.15	13,423,608	22.721	2.04	642.573	0.9123
	0.2	13,929,817	22.598	1.8526	631.23	0.8988
7 Coil	0.05	13,537,146	30.423	3.999	703.18	5.41
	0.1	15,174,066	27.481	3.7884	722	1.557
	0.1	13,038,485	21.984	2.812	675	1.764
	0.15	14,204,110	24.626	2.7905	678.25	1.1986
	0.15	13,670,268	21.984	2.603	672.24	1.28
	0.2	14,226,440	21.857	2.40587	663.43	1.0842
10 Coil	0.05	13,681,459	29.739	4.346	727.02	11.18
	0.1	13,931,965	26.810	3.5488	708	2.72
	0.1	13,266,573	21.333	3.056	686.155	3.35763
	0.15	14,271,710	23.968	3.04514	692.185	1.686
	0.15	13,266,573	21.333			
	0.2	14,596,844	21.212	2.622	672.6	1.392

* Surface Area refers to the that of the inner surface of the fuel flow domain, where all of the heat transfer occurs.

785 R. To address this, the number of coils was reduced to 5, resulting in an acceptable outlet temperature 765.1 R and maintaining a modest pressure drop of ~ 1.5 psi.

At this point, the decision had been made to use the KingTech K320 for the final design. Although initial analysis used Titanium as the nozzle material, a concurrent project drove the decision to use Haynes 282 instead. The flow paths for the air and fuel flow domains are the same between the P300 and K320; only mounting holes had to be changed, which does not affect the simulation. Differences in the results shown in Table 9 are due to the K320's higher fuel flow rate, higher air inlet temperature, and higher thermal conductivity of Haynes 282. While the fuel flow rate and thermal conductivity differences offset to maintain a similar fuel outlet temperature, the pressure drop is higher because of the K320's higher fuel flow rate. A mesh independence study was performed for the K320 simulation as well,

where increasing refinement by 20% resulted in $< 1\%$ changes for heat transfer rate, fuel outlet temperature, and pressure drop.

It should be noted that the elevated temperatures of the flow along with the small channels could potentially lead to some fluid mechanics phenomena that are difficult to capture accurately. For example, although the outlet temperature predicted by CFD is well below the boiling point of Jet A, there could potentially be a liquid/gas mixture at some point because of the high pressures the fuel will reach in the engine. Also, the flow could be turbulent at some operating points and laminar or transitional at other points. These considerations could be addressed with further studies that examine the CFD more rigorously.

Table 9: CFD secondary study results for promising candidates. Note: This includes the physical nozzle modeled as well as the flow paths, which accounts for the higher cell count compared to the preliminary studies.

	Channel Thickness (in)	No. Cells	Surface Area[a](in^2)	Heat Transfer Rate (kW)	Fuel Outlet Temperature (R)	Pressure Drop (psi)
5 Coil[b]	0.1	16,111,573	23.814	4.812	765.1	1.497
5 Coil, K320[c]	0.1	18,795,098	23.814	5.587	758.2	1.81
7 Coil[b]	0.1	18,015,322	27.173	5.01	797.1	1.42

[a] Surface Area refers to the that of the inner surface of the fuel flow domain, where most of the heat transfer occurs.
[b] The P300 nozzle is modeled using material properties for Titanium.
[c] The K320 nozzle simulation has a different air inlet temperature, fuel flow rate, and nozzle material (Haynes 282).

The straight channel and coiled & internal design results are not given here for several reasons. First, the straight channel design provided many paths for the fuel to flow and allowed the possibility of fuel to become trapped at certain locations within the nozzle and overheat. Compared to the coiled design, which only provides one path forward for the fuel, the straight channel design is inferior and was removed from consideration. Second, the CFD results for the 5 coil design demonstrate its ability to adequately heat the fuel while remaining below the maximum temperature limit, eliminating the need for more channels on the interior that would only heat the fuel more and add to the overall pressure loss.

Additionally, it would be more difficult to 3D print the design with internal channels. For these reasons, the coiled/internal design was also removed from consideration.

3.2.3 Preliminary Experiments

Setup

Preliminary experiments were conducted using PLA 3D printed nozzles, a fixed pressure head, water, and a scale to measure mass flow rate. The 3D printing process allowed manufacturability to be assessed, and small adjustments were made to wall thickness and fuel inlet/outlet geometry as a result. The experimental setup is shown in Fig. 24, where the bucket waterline height corresponds to the fixed pressure head for a given experiment. Experimental procedures will be described, but first, the supporting theory must be discussed.

Figure 24: Setup for preliminary experiments

Supporting Theory

Pressure drop is calculated from Bernoulli's principle. This equation in terms of pressure heads is given by the following equation [33]:

$$\frac{P_1}{\rho_1 g} + \frac{V_1^2}{2g} + z_1 + h_{\text{pump,u}} = \frac{P_2}{\rho_2 g} + \frac{V_2^2}{2g} + z_2 + h_{\text{turbine,e}} + h_L \tag{3.2.7}$$

where stations 1 and 2 correspond to the inlet and outlet respectively, P_i is the pressure at station i, ρ_i is the density at station i, V_i is the velocity at station i, z_i is the height of station i, $h_{\text{pump,u}}$ is the useful head delivered to the fluid by the pump, $h_{\text{turbine,e}}$ is the extracted head removed by the turbine, and h_L is the irreversible head loss from station 1 to 2.

Because this simple experimental setup does not include a pump or turbine, $h_{\text{pump,u}}$ and $h_{\text{turbine,e}}$ can be removed from the equation. Because $z_1 = z_2$ for these experiments, these can also be removed. These modifications result in the following equation:

$$\frac{P_1}{\rho_1 g} + \frac{V_1^2}{2g} = \frac{P_2}{\rho_2 g} + \frac{V_2^2}{2g} + h_L \tag{3.2.8}$$

Pressure and velocity measurements were unable to be made for these initial experiments, but mass flow rate could be measured. Substituting $V_i = \dot{m}_i/\rho_i A_i$ and $P_i = \rho_i g z_i$ gives:

$$z_1 + \frac{\dot{m}_1^2}{2g\rho_1^2 A_1^2} = z_2 + \frac{\dot{m}_2^2}{2g\rho_2^2 A_2^2} + h_L \tag{3.2.9}$$

Since the inlet and outlet areas are the same and the fluid can be assumed to be constant density, the subscript can be dropped from both A and ρ. Additionally, since $z_1 = z_2$, these can be removed. With these changes, the equation can be rewritten as:

$$h_L = \frac{1}{2g\rho^2 A^2}(\dot{m}_1^2 - \dot{m}_2^2) \tag{3.2.10}$$

While this equation is in terms of pressure heads, it can be rewritten to be in terms of pressure by multiplying by ρg:

$$\Delta P = \frac{1}{2\rho A^2}(\dot{m}_1^2 - \dot{m}_2^2) \tag{3.2.11}$$

where ΔP is the overall pressure drop. It is important to note that conservation of mass would indicate that $\dot{m}_1 = \dot{m}_2$. To be able to measure pressure drop from mass flow rate, density, and area alone, the problem must be thought of as assessing the impact of adding a thermal nozzle to the flow. The mass flow rate before adding the thermal nozzle will be greater than the mass flow rate after adding the thermal nozzle because of viscous losses in the additional flow path. Thus, the irreversible head loss from the thermal nozzle can be viewed in terms of the impact it has on mass flow rate, where $\dot{m}_1$ is the mass flow rate measured *before* adding the thermal nozzle, and $\dot{m}_2$ is the mass flow rate measured *after* adding the thermal nozzle.

Experimental Procedure

The height from the ground is measured for each of the following locations in each experiment: the waterline in the bucket and the nozzle inlet/outlet. Each experiment consists of two trials, where the nozzle is either attached or detached for a given waterline height / head pressure. This allows the mass flow rates for each case to be measured, $\dot{m}_1$ and $\dot{m}_2$.

To measure mass flow rate, the initial mass of the bucket is measured ($m_{b,i}$), water is allowed to flow for $t = 180$ seconds, then the final mass of the bucket is measured ($m_{b,f}$). The mass flow rate can be calculated simply as:

$$\dot{m} = \frac{m_{b,i} - m_{b,f}}{t} \tag{3.2.12}$$

The results of $\dot{m}_1$ and $\dot{m}_2$ can then be used to find the pressure drop using the method outlined in the previous section.

CFD Setup

The CFD setup remained the same as previously described, except there was no air flow domain, just the fuel flow domain, where the fluid continua was water and the mass flow rate at the inlet was equal to the experimental mass flow rate *without* the nozzle attached. Additionally, the coupled energy solver was turned off because heat transfer did not need to be accounted for.

Preliminary Results and CFD Comparison

Table 10 shows the experimental results for $\dot{m}_1$ and $\dot{m}_2$ along with the calculated values for ΔP. The CFD results are also shown in this table, where $\dot{m}_{inlet}$ and $\dot{m}_{outlet}$ correspond to the inlet and outlet of the thermal nozzle respectively. For all cases, the inlet boundary condition is $\dot{m}_{inlet} = \dot{m}_1$. The pressure drop is obtained for two outlet conditions: $\dot{m}_{outlet} \approx \dot{m}_2$, where results are taken mid-simulation, and $\dot{m}_{outlet} \approx \dot{m}_{inlet}$ at the end of the simulation.

For the highest head pressure case when $\dot{m}_{outlet} \approx \dot{m}_2$, the ΔP from the CFD results has only a 1.18% difference from experimental results. As head pressure decreases, however, the ΔP from the CFD results becomes less accurate regardless of when in the simulation ΔP is recorded. Since the fuel will be pumped through the nozzle at much higher pressures than 1.527 psi and the CFD simulations appear to be more accurate at higher pressures, it can be concluded that the CFD results accurately match the experimental results.

Final Design Selection

After performing CFD studies and experimental trials to verify numerical results, it was decided that the 5 coil design was the best and met the key metrics of manufacturability, heat transfer rate, fuel outlet temperature, and pressure drop.

Table 10: Experimental vs. CFD results for 5 coil design

Head Pressure (psi)	$\dot{m}_1$ Exp. (lb/s)	$\dot{m}_{inlet}$ CFD (lb/s)	$\dot{m}_2$ Exp. (lb/s)	$\dot{m}_{outlet}$ CFD (lb/s)	ΔP Exp. (psi)	ΔP CFD (psi)	% Diff.
1.527	0.008696	0.008696	0.005120	0.008680	0.1738	0.2054	18.15 %
1.527	0.008696	0.008696	0.005120	0.005119*	0.1738	0.171786	1.18 %
1.256	0.007912	0.007912	0.004544	0.007620	0.16951	0.147813	12.80 %
1.256	0.007912	0.007912	0.004544	0.004560*	0.16951	0.174252	2.80 %
1.003	0.007226	0.007226	0.003895	0.006959	0.16666	0.149961	24.90 %
1.003	0.007226	0.007226	0.003895	0.003892*	0.16666	0.125162	10.02 %
0.713	0.005781	0.005781	0.003037	0.005538	0.15919	0.104458	34.38 %
0.713	0.005781	0.005781	0.003037	0.003038*	0.15919	0.0865625	45.62 %
0.353	0.002156	0.002156	0.001788	0.002029	0.14597	0.0246041	83.14 %
0.353	0.002156	0.002156	0.001788	0.001789*	0.14597	0.0233494	84.00 %

* Results were obtained mid-simulation where $\dot{m}_1 = \dot{m}_{inlet}$ and $\dot{m}_2 \approx \dot{m}_{outlet}$ (see Fig. 25a).

3.3 Engine Cycle Analysis

3.3.1 Parametric Cycle Analysis Methodology and Results

Cycle analysis was performed according to the procedure outlined in section 2.1.5. Initial analysis was done on the JetCat P300, which has specifications as shown in Table 11. As discussed in section 3.1, a similar turbojet, the KingTech K320, was selected for the final design because of its availability. Unfortunately, the K320 has fewer specifications available from the manufacturer or in literature, so some quantities had to be estimated from the P300, as shown in Table 12.

Table 11: JetCat P300-Pro Specifications [14]

π_c	$\dot{m}_0$ (lb/s)	$\dot{m}_f$ (lb/s)	F_{max} (lbf)
3.55	1.102	0.02917	67.44

Table 12: KingTech K320 Specifications [14, 1]

π_c*	$\dot{m}_0$ (lb/s)*	$\dot{m}_f$ (lb/s)	F_{max} (lbf)
3.55	1.102	0.032	70.57

* These quantities estimated from P300 values.

Component efficiencies of LOT 3 (see Table 2 in section 2.1.5) were used for all compo-

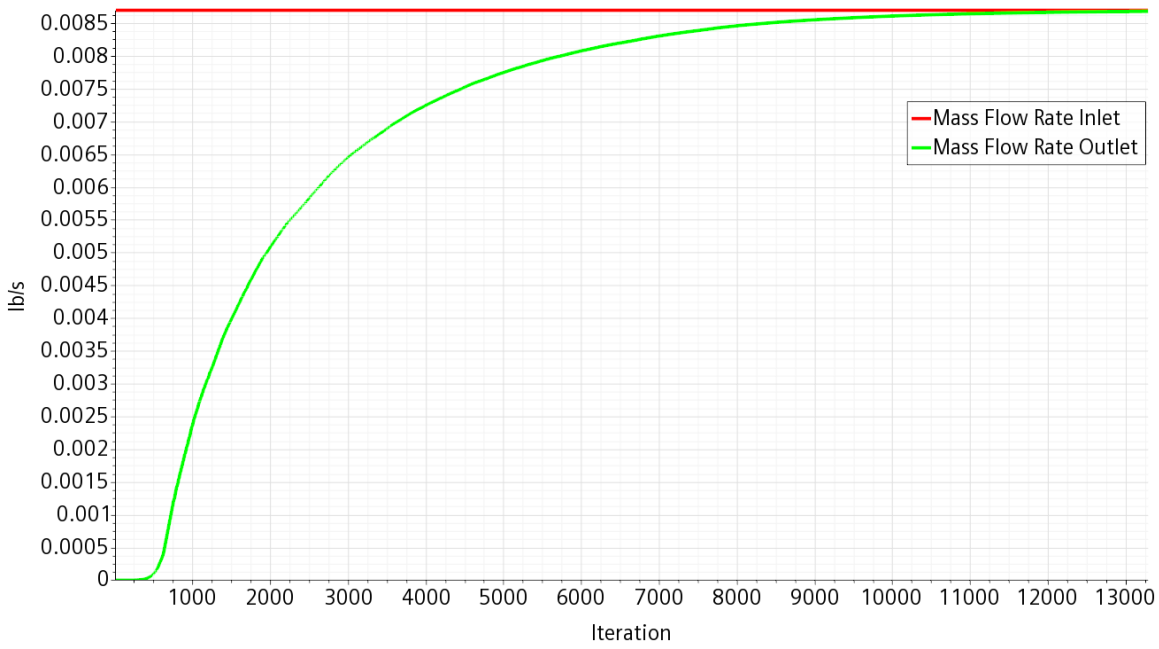

(a) Mass flow rate vs. CFD iterations. $\dot{m}_{outlet} \approx \dot{m}_2$ at iteration 2015.

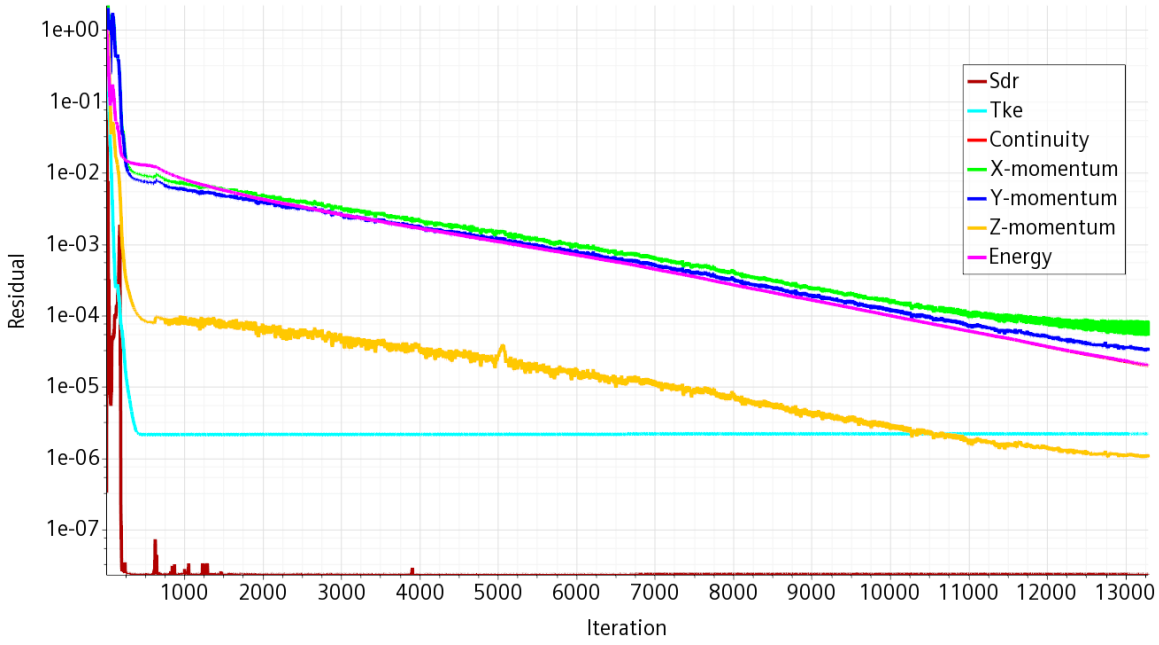

(b) Residuals for the same simulation.

Figure 25: CFD with Fuel Flow Domain only (using water as fluid) to match 5 Coil preliminary experiment, head pressure = 1.527 psi.

nents except the burner, which began at LOT 1 and was scaled until the resulting thrust, F, matched F_{max} from the K320 specifications.

Once cycle analysis without fuel preheat is performed, T_{t5} can be used as the air inlet temperature in the thermal nozzle CFD simulation. From the CFD results, we obtain $\dot{Q}_{f,noz}$ and $T_{f,out}$. With these quantities in hand, the process for adding fuel preheat to the cycle analysis, as described in section 2.1.6, is followed.

3.3.2 Engine Performance Analysis Methodology and Results

Once PCA was performed, EPA calculations were made following the procedure outlined in section 2.1.5. During experimental trials, the stick positions of 20%, 40%, 60%, 80%, and 100% were used as the throttle settings. Corrections had to be made to determine the correct T_{t4} because the K320 engine control unit (ECU) uses either a half or full exponential throttle curve. These correspond to the control unit stick positions as given in Table 13. These values for half and full expo can be correlated to the stick position with an $R^2 = 1$ using the polynomial expressions in Eqs. 3.3.1 and 3.3.2 respectively.

Table 13: Stick position vs. % of total thrust [30]

Stick Position (Throttle)	0% (Idle)	25%	50%	75%	100%
Half Expo % of total thrust	Idle Thrust	16%	38%	66%	100%
Full Expo % of total thrust	Idle Thrust	6%	25%	56%	100%

$$\%_{thrust} = 0.48(\%_{stick})^2 + 0.52(\%_{stick}) \tag{3.3.1}$$

$$\%_{thrust} = \frac{15}{75}(\%_{stick})^4 - \frac{32}{75}(\%_{stick})^3 + \frac{19}{15}(\%_{stick})^2 - \frac{4}{75}(\%_{stick}) \tag{3.3.2}$$

The T_{t4} used for each EPA calculation at the given throttle setting is given by Eq. 3.3.3, where $T_{t4,idle}$ is calibrated by matching the output thrust from EPA to the experimental idle thrust. From there, the procedure from 2.1.5 is followed.

$$T_{t4} = T_{t4,idle} + (\%_{thrust})(T_{t4R} - T_{t4,idle}) \tag{3.3.3}$$

3.4 Experimental Evaluation

3.4.1 Setup

The KingTech K320 is mounted on the 80/20 T-slot aluminum beams as shown in Fig. 26, with a pivot point at the base. This is connected to a horizontal bar that transfers the force produced by the turbojet to a 500 lb load cell (Futek FSH03891), which measures that force and records it to the connected computer via USB. This load cell measures with accuracy of ±0.001 lbf, and data is logged at a rate of 15 Hz. Simple moment arm calculations are then used to adjust the measured force on the load cell to the actual thrust produced by the turbojet.

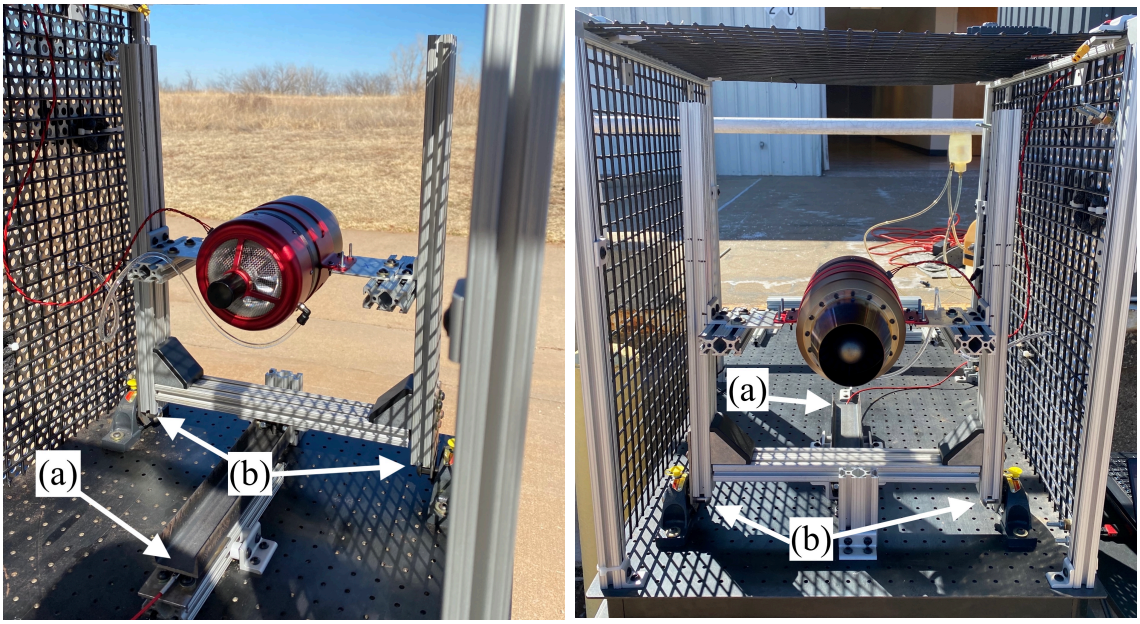

Figure 26: Experimental setup, original nozzle attached. Load cell (a) placed equal distance from axle (b) as the turbojet to simplify force measurement and calculations.

Mass flow rate is measured using a scale that is placed underneath the fuel tank, where a video camera records the value over time (see Fig. 27). The scale measures with an accuracy of 0.1g with a refresh rate of ~ 4 Hz. The recorded mass versus time is converted to a mass flow rate using simple calculations.

The fuel outlet temperature is measured using a simple thermocouple device placed inline

Figure 27: Experimental setup for measuring mass flow rate of fuel.

between the nozzle exit and the engine inlet, as shown in Fig. 28. A video camera records the temperature at each throttle setting. This setup could likely be improved in the future to increase the accuracy and response time of the measurements.

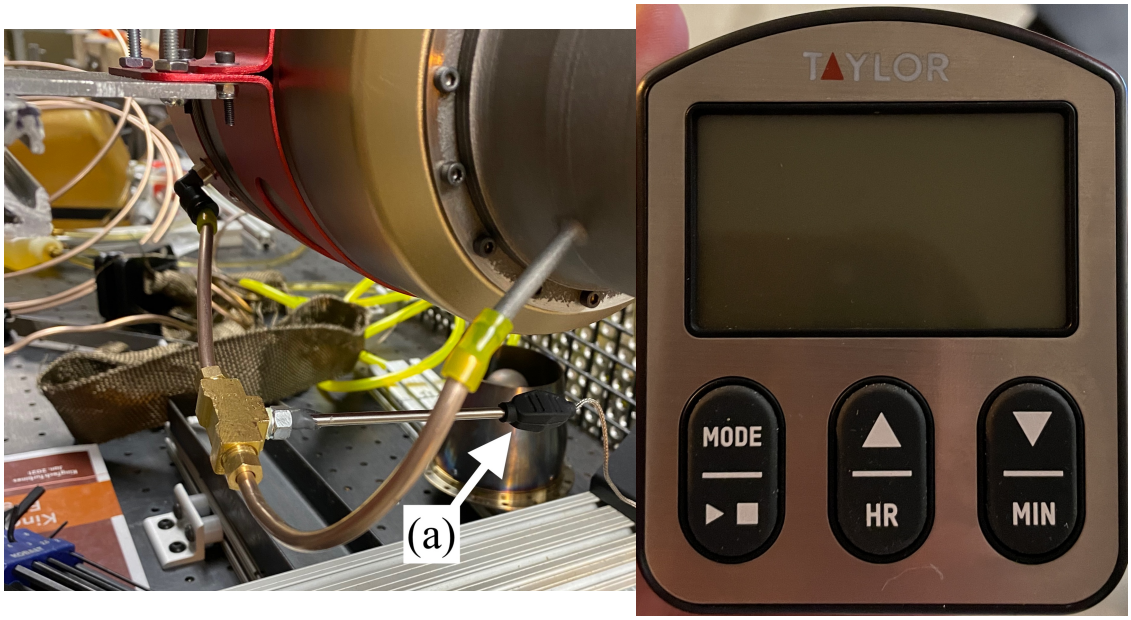

Figure 28: Simple temperature measurement device, with the probe inline at (a).

The atmospheric temperature and pressure are recorded after each trial using the device

shown in Fig. 29. These measurements are used in data analysis to correct the measured F and $\dot{m}_f$ values to sea-level static conditions, enabling comparison with EPA predictions.

Figure 29: Device to measure temperature and pressure after each trial.

The throttle is controlled using a servo tester (Fig. 30), which has a PWM range of 1000 - 2000. The engine idle is at 1100, so 0% - 100% throttle corresponds to the 1100 - 2000 range.

Figure 30: Throttle controller

3.4.2 Procedures

The procedure for running an experimental trial is as follows:

1. Begin data logging for measurement devices.
2. Initiate startup sequence for the K320.
3. Raise throttle to 20% (1280 on PWM controller), then hold for 5-10 seconds.
4. Raise throttle to 40%, 60%, 80%, and 100%, holding for 5-10 seconds at each.

5. Shut down engine.

6. Record the temperature and pressure for that trial to calculate corrected F and $\dot{m}_f$.

At each throttle setting, a hand signal is flashed to the fuel flow rate camera, indicating which throttle percentage and the start point for measuring fuel flow rate. Just before increasing throttle, another hand signal is flashed to the camera, indicating the stop point for measuring that throttle setting's fuel flow rate. This defines a clear time period that can be used in post-processing to enter mass measurements (g) versus time (ms) at a specific throttle setting into a spreadsheet.

The data is gathered for several trials to allow for statistical analysis, but the sample size is small for each case. Therefore, a t-distribution is used to predict whether there is a statistical difference between the mean values for each quantity of the thermal nozzle samples with and without fuel preheat. The result of most interest is whether the thermal nozzle's TSFC with fuel preheat is statistically lower than its TSFC without fuel preheat.

3.4.3 Data Analysis

Two methods are used to calculate the average fuel flow rate at a throttle setting: the average of the entire time period ($\Delta m_f/\Delta t$) and the average of the differential mass flow rates ($\sum \delta\dot{m}_f/n$, where n is the number of differential measurements). In practice, these values for $\dot{m}_f$ are very similar, and an example of these calculations for a certain throttle setting is shown in Table 14.

For thrust measurements, the load cell had data logging capabilities that made recording the data simple. An example of output from one of the experimental trials is shown in Fig. 31. At each throttle setting, the average force output is recorded for the trial thrust value. The set of trial averages is used as the sample for estimating the population mean.

After $\dot{m}_{f,avg}$ and F_{avg} have been calculated for each trial and throttle setting, they are corrected to sea-level static conditions, as described in section 2.1.5, using the pressure and temperature measurements from each trial. This makes results from different test conditions

Table 14: Example of fuel flow rate spreadsheet calculations for 60% throttle. The two $\dot{m}_{f,avg}$ calculation methods provide very similar results.

	Time (ms)	m_{tank} (g)	$\delta\dot{m}_f$ (g/s)
	82393	-271.9	
	83527	-282.7	9.524
	84628	-292.8	9.173
	85628	-301.1	8.300
	86697	-309.6	7.951
	87897	-319.3	8.083
	88965	-327.3	7.491
$\dot{m}_{f,avg}$ (g/s)		8.430	8.420

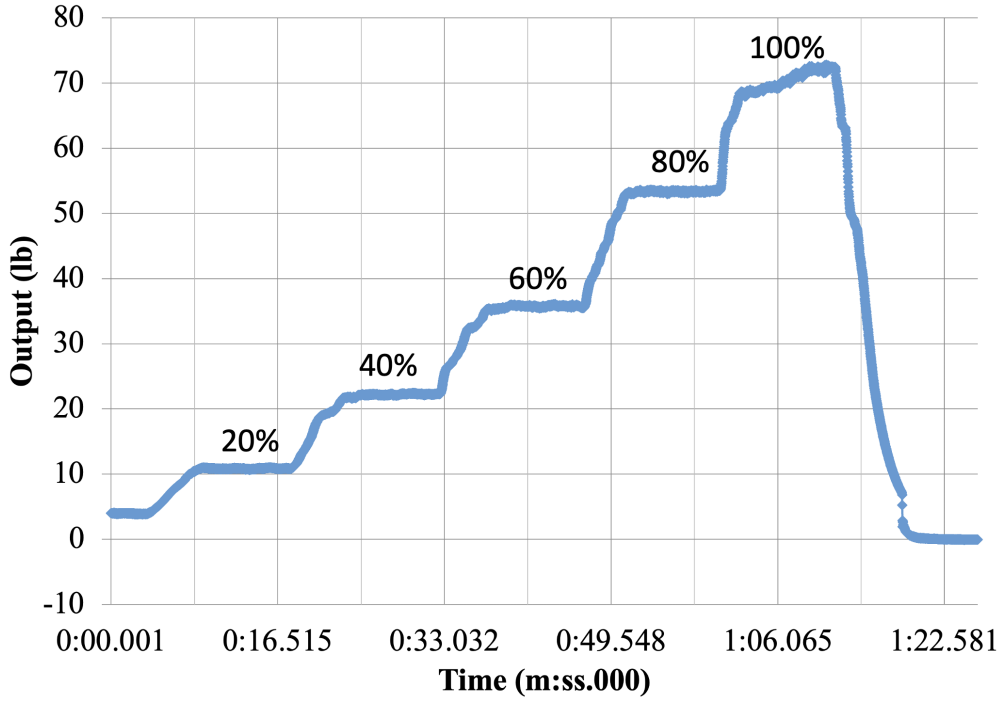

Figure 31: Example of load cell data logging from an experimental trial.

comparable to each other and the analytical EPA values. Finally, the corrected values F_c and $\dot{m}_{fc}$ can be used to calculate TSFC for each trial by dividing $\dot{m}_{fc}/F_c$ and ensuring the units are consistent.

Statistical Analysis

Once the data has been gathered, corrected, and TSFC calculated, statistical analysis can be performed to compare the results between the thermal nozzle with and without fuel running

through it. This can be done using hypothesis testing about differences in population means. A summary of this method as used in this study is given in Table 15, where the H_0 is the null hypothesis, H_1 is the alternative hypothesis, μ_i is the population mean corresponding to sample i, $\delta_0 = 0$ in this study to indicate a difference in population means, t is the test statistic, $\bar{Y}_i$ is the sample mean for sample i, n_i is the sample size of sample i, σ^2 is variance, *df* is degrees of freedom, α is the probability of making a type I error (rejecting H_0 when it is true), and $s_{\bar{Y}_1-\bar{Y}_2}$ is the standard error of the estimator, defined by Eqn. 3.4.1.

Table 15: Difference in population means [23]

Hypothesis	Test Statistic	Rejection Region	Conditions & Definitions
$H_0 : \mu_1 - \mu_2 = \delta_0$ $H_1 : \mu_1 - \mu_2 > \delta_0$	$t = \frac{(\bar{Y}_1-\bar{Y}_2)-\delta_0}{s_{\bar{Y}_1-\bar{Y}_2}}$	$t \geq t_{\alpha,df}$	1. Random Samples 2. Independent Samples 3. Pops. 1 & 2 normally distributed
$H_0 : \mu_1 - \mu_2 = \delta_0$ $H_1 : \mu_1 - \mu_2 < \delta_0$		$t \leq -t_{\alpha,df}$	4. $df = n_1 + n_2 - 2$

$$s_{\bar{Y}_1-\bar{Y}_2} = \begin{cases} \sqrt{s_p^2\left(\frac{1}{n_1}+\frac{1}{n_2}\right)} & , \sigma_1^2 = \sigma_2^2 \\ \sqrt{\frac{s_1^2}{n_1}+\frac{s_2^2}{n_2}} & , \sigma_1^2 \neq \sigma_2^2 \end{cases} \tag{3.4.1}$$

When population variances are equal, $s_{\bar{Y}_1-\bar{Y}_2}$ is better estimated using a pooled variance, s_p^2, defined by Eqn. 3.4.2:

$$s_p^2 = \left(\frac{(n_1-1)s_1^2 + (n_2-1)s_2^2}{n_1+n_2-2}\right) \tag{3.4.2}$$

Naturally, this gives rise to the question of whether population variances are equal. This can be done using hypothesis testing about a difference in population variances, a summary of which is given in Table 16.

With the data in hand for sample means and variances of the thermal nozzle experiments, these statistical methods can be employed to determine whether the mean TSFC of the thermal nozzle with fuel running through it is statistically greater than, less than, or equal

Table 16: Difference in population variances [23]

Hypothesis	Test Statistic	Rejection Region	Conditions & Definitions
$H_0 : \sigma_1^2 = \sigma_2^2$ $H_1 : \sigma_1^2 \neq \sigma_2^2$	$F = \frac{s_1^2}{s_2^2}$	$F \leq \frac{1}{F_{\frac{\alpha}{2},n_2-1,n_1-1}}$ $F \geq F_{\frac{\alpha}{2},n_1-1,n_2-1}$	1. Random Samples 2. Independent Samples 3. Pops. 1 & 2 normally distributed 4. ndf[a]$= n_1 - 1$ 5. ddf[b]$= n_2 - 1$

[a] *ndf* is numerator degrees of freedom for F test statistic.
[b] *ddf* is denominator degrees of freedom for F test statistic.

to the nozzle without fuel running through it.

3.4.4 Test Matrix

The test matrix for this study is shown in Table 17. All throttle settings and fuel choices are first tested with the original nozzle mounted to validate EPA predictions. Once these have been obtained, the same tests are performed with the thermal nozzle mounted, first without fuel running through it (baseline), then with fuel running through it. From there, the results will be compared and analyzed.

Table 17: Test Matrix for Experimental Evaluation – Will be run for both Jet A and Diesel

	Throttle %	Original	Thermal (baseline)	Thermal
F (lb)	20%			
	40%			
	60%			
	80%			
	100%			
$\dot{m}_f$ (lb/s)	20%			
	40%			
	60%			
	80%			
	100%			
TSFC (1/hr)	20%			
	40%			
	60%			
	80%			
	100%			
$T_{f,out}$ (R)	20%	-	-	
	40%	-	-	
	60%	-	-	
	80%	-	-	
	100%	-	-	

CHAPTER IV

RESULTS

The results in this section are divided into analytical results from PCA and EPA, experimental results from the K320 with the original nozzle, and experimental results from the K320 with the thermal nozzle.

4.1 PCA & EPA Results

4.1.1 PCA Results

Table 18 shows some key results of the parametric cycle analysis for both the original and thermal nozzle. Most importantly, TSFC is predicted to be reduced by a promising 2.073% with the thermal nozzle mounted, although this comes at the expense of specific thrust, which is predicted to be reduced by 0.476%. The design point for these values is full throttle because that is what was available from the engine manufacturer for reference values.

Table 18: PCA results for KingTech K320

Quantity	Original	Thermal	% Diff.
T_{t4} (R)	2260.356	2260.356	0%
T_{t5} (R)	2038.369	2038.211	7.77E-3%
TSFC (1/hr)	1.631	1.597	-2.0726%
$F/\dot{m}_0$ (lbf/(lbm/s))	64.0219	63.7169	-0.4764%

4.1.2 EPA Results

Next, EPA results show the predicted performance of the engine with and without fuel preheating at different throttle settings. While the results for half expo and full expo appear

different in Fig. 32, the difference is simply that they represent different T_{t4}'s for a given stick throttle percentage. An interesting trend is that TSFC appears to be reduced more at higher throttle settings. The same trend is shown for specific thrust except at 20% throttle, where it is reduced by much more. More detailed results and percentages are shown in Table 19.

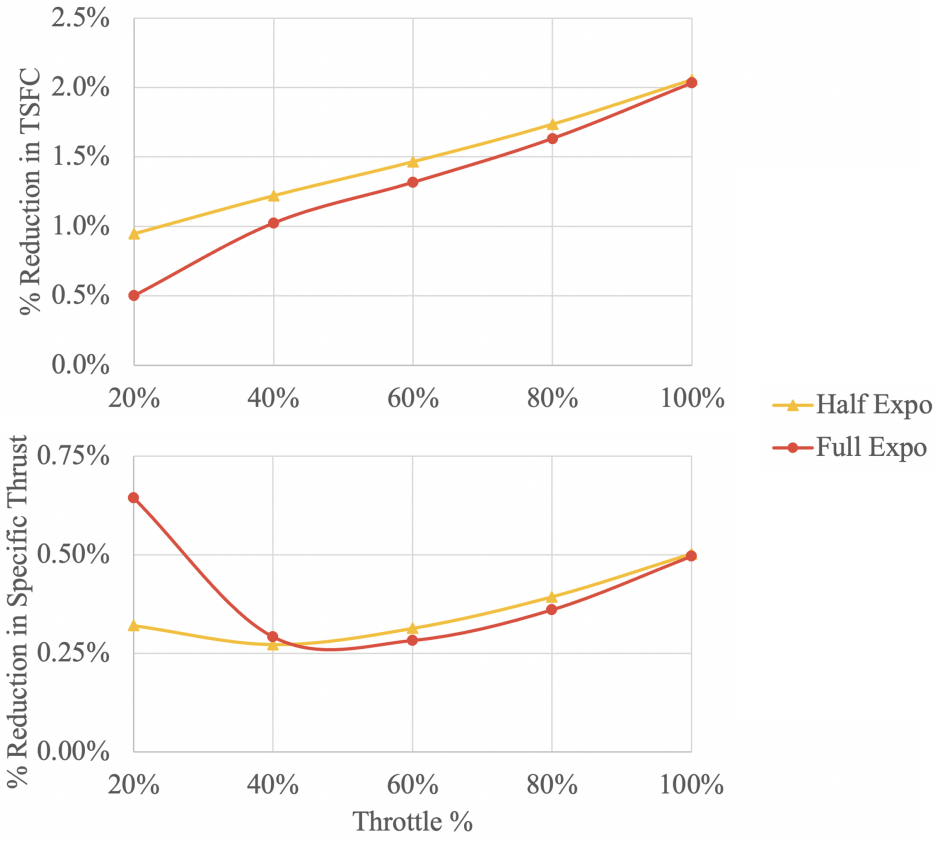

Figure 32: EPA results for TSFC and $F/\dot{m}_0$ – original vs. thermal nozzle

4.2 Original Nozzle Results

Experimental results for the K320 with the original nozzle and Jet A are presented and compared with EPA predictions in Figure 33 and Table 20. From these results, it is clear that neither throttle curve matches the experimental results perfectly for the F and $\dot{m}_f$ values. However, the full expo curve matches experimental results quite well for TSFC values from 40%-100% throttle.

Table 19: EPA results for K320

		Half Expo			Full Expo		
	Throttle	Original	Thermal	% Diff.	Original	Thermal	% Diff.
F (lb)	20%	16.015	15.964	-0.321%	9.035	8.977	-0.645%
	40%	26.139	26.067	-0.273%	18.427	18.374	-0.292%
	60%	37.828	37.709	-0.313%	30.413	30.327	-0.283%
	80%	52.261	52.056	-0.393%	46.590	46.422	-0.360%
	100%	70.572	70.218	-0.501%	69.644	69.298	-0.496%
$\dot{m}_f$ (lb/s)	20%	0.01017	0.01004	-1.263%	0.00856	0.00846	-1.142%
	40%	0.01340	0.01320	-1.489%	0.01087	0.01072	-1.312%
	60%	0.01784	0.01752	-1.774%	0.01496	0.01472	-1.595%
	80%	0.02385	0.02334	-2.121%	0.02144	0.02101	-1.986%
	100%	0.03197	0.03116	-2.548%	0.03155	0.03075	-2.517%
TSFC (1/hr)	20%	2.287	2.265	-0.946%	3.411	3.394	-0.501%
	40%	1.846	1.823	-1.220%	2.123	2.101	-1.023%
	60%	1.697	1.673	-1.465%	1.771	1.747	-1.316%
	80%	1.643	1.614	-1.735%	1.656	1.629	-1.632%
	100%	1.631	1.597	-2.057%	1.631	1.598	-2.031%
$F/\dot{m}_0$ (lbf/(lbm/s))	20%	17.985	17.927	-0.321%	10.270	10.204	-0.645%
	40%	28.502	28.424	-0.273%	20.573	20.513	-0.292%
	60%	39.431	39.307	-0.314%	32.651	32.559	-0.283%
	80%	51.228	51.026	-0.393%	46.797	46.628	-0.361%
	100%	64.022	63.701	-0.502%	63.422	63.107	-0.496%
$T_{f,out}$ (R)	20%	-	577.026	-	-	558.843	-
	40%	-	611.078	-	-	584.601	-
	60%	-	653.222	-	-	626.452	-
	80%	-	703.457	-	-	684.127	-
	100%	-	761.783	-	-	758.973	-

The 20% throttle predictions for TSFC are unreliable, which could have several explanations. First, the 20% results could be less accurate because they are the furthest from the calibration point of full throttle. It is very likely that not all of the assumptions for EPA hold at such a low throttle setting. For example, the turbine is almost certainly not choked, making this assumption and its dependencies (like having a constant π_t and τ_t) invalid. Additionally, the assumption of constant γ_t and $c_{p,t}$ for varying T_{t4} is clearly inaccurate for such a low throttle setting, where the T_{t4} is predicted to be about 1160 R lower than the design point $T_{t4,max} = 2260$ R. Regardless of the causes for inaccuracy, it is also worth noting that results for 20% throttle are likely irrelevant for most scenarios, where sustained throttle

settings like takeoff or cruise occur at higher thrust values.

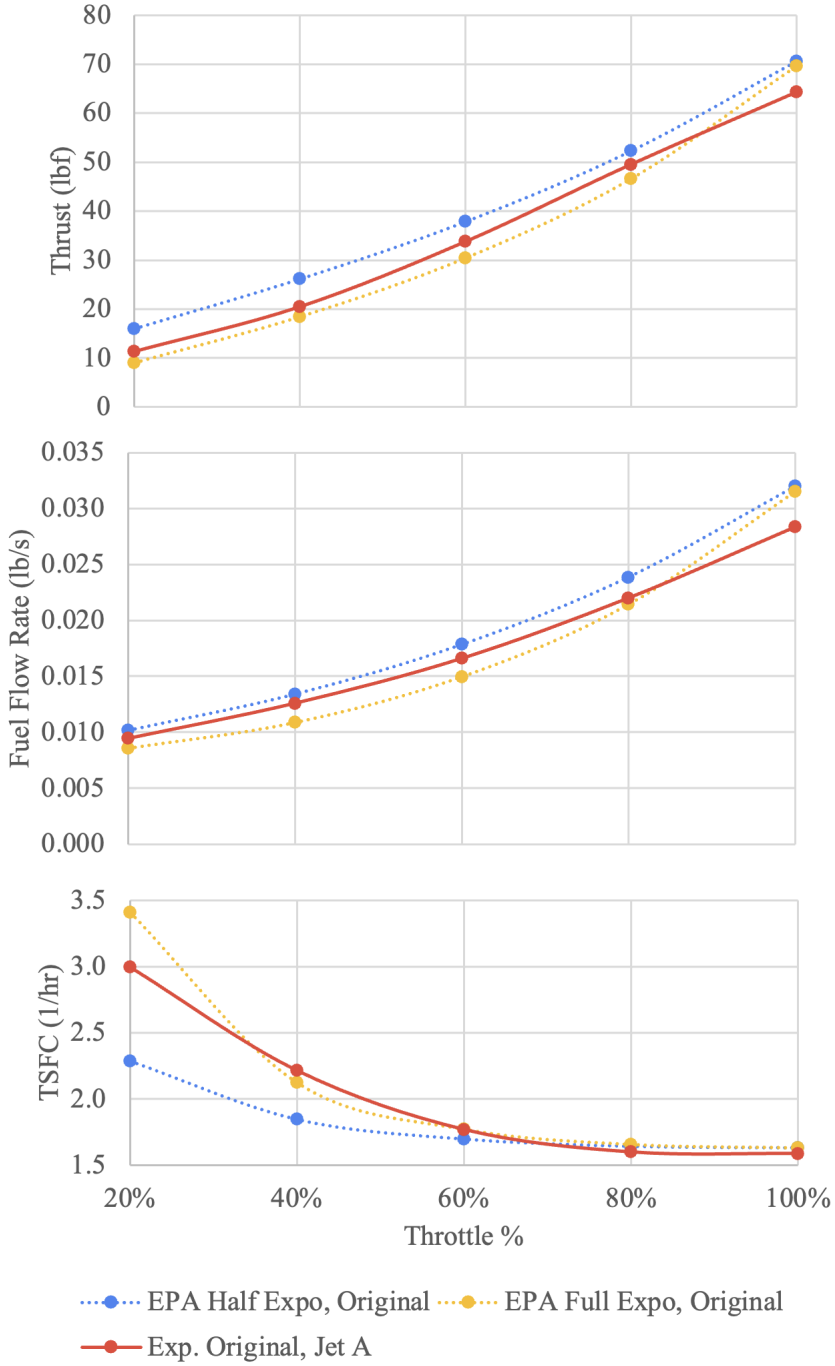

Figure 33: EPA vs. Experimental Results – Original Nozzle, Jet A

Experimental results for the original nozzle with *diesel* are shown in Figure 34 and Table 21. Similar observations can be made for diesel results as for Jet A, although it appears the values for F and $\dot{m}_f$ are slightly higher for diesel.

Table 20: EPA (Half & Full Expo) vs. Experimental Results for Original Nozzle, Jet A

	Throttle	EPA Half	EPA Full	Exp.	% Diff. Half	% Diff. Full
F (lb)	20%	16.015	9.035	11.343	41.19%	-20.34%
	40%	26.139	18.427	20.466	27.72%	-9.96%
	60%	37.828	30.413	33.744	12.10%	-9.87%
	80%	52.261	46.590	49.495	5.59%	-5.87%
	100%	70.572	64.251	64.251	9.84%	8.39%
$\dot{m}_f$ (lb/s)	20%	0.01017	0.00856	0.0094	7.84%	-9.26%
	40%	0.01340	0.01087	0.0126	6.58%	-13.58%
	60%	0.01784	0.01496	0.0166	7.57%	-9.78%
	80%	0.02385	0.02144	0.0220	8.50%	-2.48%
	100%	0.03197	0.03155	0.0283	12.84%	11.34%
TSFC (1/hr)	20%	2.287	3.411	2.993	-23.61%	13.94%
	40%	1.846	2.123	2.213	-16.60%	-4.08%
	60%	1.697	1.771	1.769	-4.04%	0.11%
	80%	1.643	1.656	1.599	2.73%	3.57%
	100%	1.631	1.631	1.587	2.73%	2.72%

Table 21: EPA (Half & Full Expo) vs. Experimental Results for Original Nozzle, Diesel

	Throttle	EPA Half	EPA Full	Exp.	% Diff. Half	% Diff. Full
F (lb)	20%	16.015	9.035	10.976	45.91%	-17.68%
	40%	26.139	18.427	21.400	22.15%	-13.89%
	60%	37.828	30.413	35.565	6.36%	-14.49%
	80%	52.261	46.590	53.960	-3.15%	-13.66%
	100%	70.572	64.251	66.114	6.74%	5.34%
$\dot{m}_f$ (lb/s)	20%	0.01017	0.00856	0.0090	12.97%	-4.94%
	40%	0.01340	0.01087	0.0124	7.91%	-12.50%
	60%	0.01784	0.01496	0.0173	2.82%	-13.76%
	80%	0.02385	0.02144	0.0240	-0.62%	-10.68%
	100%	0.03197	0.03155	0.0304	5.11%	3.71%
TSFC (1/hr)	20%	2.287	3.411	3.052	-25.07%	11.76%
	40%	1.846	2.123	2.159	-14.52%	-1.69%
	60%	1.697	1.771	1.814	-6.43%	-2.39%
	80%	1.643	1.656	1.655	-0.71%	0.10%
	100%	1.631	1.631	1.711	-4.67%	-4.68%

4.3 Thermal Nozzle Results

Caution was taken when performing initial trials with the thermal nozzle to ensure proper operation before running any fuel through it. During these initial runs, elevated exhaust gas temperatures (EGT) were observed, indicating potential back pressure issues. EGT

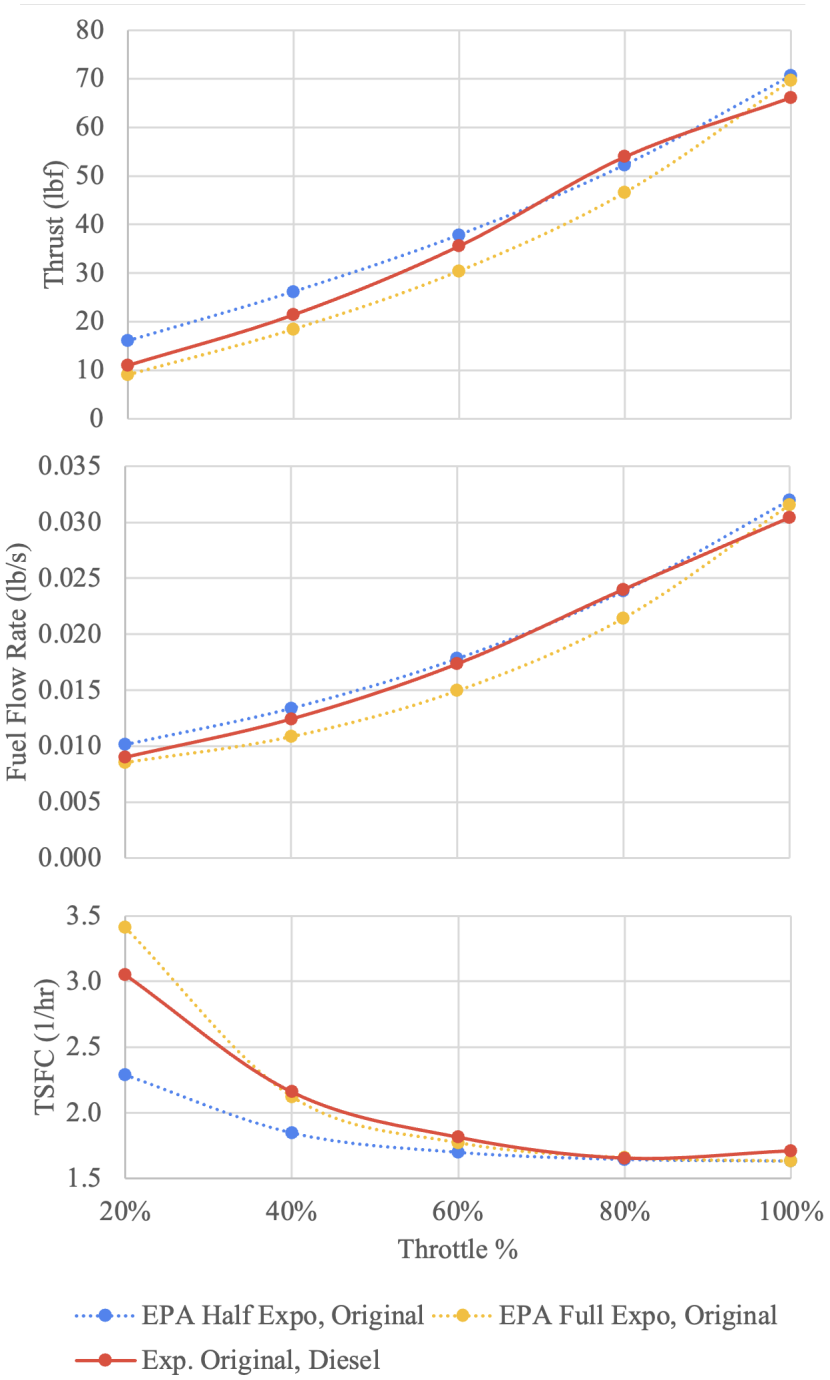

Figure 34: EPA vs. Experimental Results – Original Nozzle, Diesel

data from the KingTech engine control unit (ECU) was gathered for both the original and thermal nozzles when running the engine up to idle, where results are shown in Fig. 35. The original nozzle EGT only reaches about 400 C (1211 R) at idle, whereas the thermal nozzle reaches about 880 C (2075 R), which is close to the original nozzle EGT at full throttle.

(a) Original Nozzle (b) Thermal Nozzle

Figure 35: KingTech ECU data for exhaust gas temperature (red) when running the engine up to idle thrust

Despite the similarities between the P300 and the K320, it is clear that the flow characteristics between the two are different. The flow area through the nozzle, shown in Fig. 36, is likely too small for the K320. It is possible that adjusting the blockage area of the exit guide vanes or increasing the exit area through modification of the nose cone could make this nozzle operational without having to print a second revision. For this study, however, experimental measurements were not gathered to avoid causing engine damage.

Figure 36: Exit area for the thermal nozzle likely too small for the K320

CHAPTER V

CONCLUSION

Analytical predictions from PCA and EPA show that TSFC is improved at every throttle setting, where higher throttle settings corresponds to higher percentage improvement. A promising 2.07% improvement in TSFC is shown at full throttle, although specific thrust is reduced by 0.48%. These results are predicted by:

- CFD, where preliminary validation has been performed through pressure drop experiments.
- PCA & EPA, which have been validated through experimental trials with the original nozzle.
- ε-NTU model and h_{PR} adjustments, which have not yet been validated through experimental trials with the thermal nozzle.

To evaluate the net benefit of adding the thermal nozzle, other factors must be considered such as added weight, cost, and MTBO. The promising analytical predictions of this study show that continued research into the thermal nozzle is warranted.

5.1 Recommendations for Future Work

Future studies could focus on several topics, including completion of experimental validation, weight reduction, scaling effects, improved CFD fidelity, and combustor/control unit modification to optimize the engine for fuel preheating.

Experimental Validation: Completing the experimental validation could involve modification of the currently printed nozzle to open up the exit flow area. A second revision could either be based on the original nozzle geometry to ensure adequate flow area, or refinements could be made to the existing thermal nozzle geometry to maintain the original intent of the P100 nozzle to improve the engine's thrust-to-weight ratio.

Weight Reduction: Because weight was not a major consideration in this study, the final nozzle weighs 1.76 lb, whereas the original nozzle weighs only 0.54 lb. There are several clear opportunities for weight reduction. First, the thickness of the thermal nozzle walls is much thicker than the original, so this could be reduced throughout. Second, the exit guide vanes are currently solid, but they could be made hollow to reduce weight. Finally, alternative materials could be explored, as Haynes 282 was chosen for reasons related to a concurrent project. The cooling provided to the nozzle by the fuel could potentially allow for unconventional nozzle materials to be used like aluminum. Even if the fuel cooling is not sufficient, using a material like titanium would significantly reduce the nozzle weight because its density is 0.16 lb/in^3, almost half the 0.30 lb/in^3 density of Haynes 282. This change alone would reduce the existing geometry weight to 0.94 lb.

Scaling Effects: While the nozzle in this study was designed for a 70 lbf turbojet, the thermal nozzle concept could be applied to other engine sizes as well, where various scaling effects could be studied. These include differences in exhaust gas temperatures, heat transfer surface areas, fuel residence time within the nozzle, and flow rates for exhaust gas and fuel.

Improved CFD Fidelity: As mentioned in section 3.2.2, there are additional complexities that could come into play depending on the pressure and flow rate of the fuel as it runs through the nozzle. Further improvements to the CFD modeling could be made to address these considerations and improve the fidelity of the results.

Combustor & Control Unit Modification: As mentioned in section 2.2.2, the combustor rate of reaction and atomization characteristics can be affected by the elevated fuel temperature. Additionally, the vaporization tubes within the engine are sized for fuel that has not been preheated. Consequently, it is possible that the combustor will require modifications to achieve optimal efficiency in the presence of the thermal nozzle.

Furthermore, the stock ECU adjusts the fuel flow rate without any knowledge of the preheated fuel. As shown in previous analysis, however, the thermal nozzle causes a lower $\dot{m}_f$ to be required to reach the same T_{t4}. Having a custom control unit could allow the fuel outlet temperature to contribute to the calculated fuel pump setting, or alternative control curves could be calibrated to account for the presence of the thermal nozzle. Having the custom ECU could also unlock other engine modifications beyond the scope of this study.

REFERENCES

[1] *K-320G4+ [K320G4] - $4,150.00 : KingTech Turbines, KingTech Turbines*, December 2021.

[2] Aero & Air, *Engine Fuel Systems Part 1 - Aircraft Gas Turbine Engines #19*, April 2020, Directors: _:n964.

[3] Aaron Alexander, *Practical CFD: Module 3, Lecture 2*, Presenters: _:n1386.

[4] ———, *Quick Question on Mesh Independence*, January 2022.

[5] John D. Anderson and John D. Anderson, *Fundamentals of aerodynamics*, 5th ed ed., Anderson series, McGraw-Hill, New York, 2011, OCLC: ocn463634144.

[6] Caltech, *Law of the Wall*, An Internet Book on Fluid Dynamics, January 2022.

[7] Chevron, *Diesel Fuels Technical Review*, Tech. report.

[8] Fabíola Paula Costa, Luiz Henrique Lindquist Whitacker, Cleverson Bringhenti, Jesuino Takachi Tomita, Gustavo Bonolo Campos, Luiz Eduardo Nunes Almeida, and Diogo Ferraz Cavalca, *An overview of small gas turbine engines*, (2019), 12 (en).

[9] Thomas Coulon, Riley Johnson, Lauren Jones, Michael Mines, Grant Schumacher, and Colton Swart, *Thrust-to-Weight Improvement of JetCat P100-RX Turbojet Engine*, 18 (en).

[10] Irvin Glassman and Richard A. Yetter, *Combustion*, 4th ed ed., Academic Press, Amsterdam ; Boston, 2008 (en).

[11] W. E. Harrison, K. E. Binns, S. D. Anderson, and R. W. Morris, *High Heat Sink Fuels for Improved Aircraft Thermal Management*, July 1993, p. 932084 (en).

[12] S. P. Heneghan, S. Zabarnick, D. R. Ballal, and W. E. Harrison, III, *JP-8+100: The Development of High-Thermal-Stability Jet Fuel*, Journal of Energy Resources Technology **118** (1996), no. 3, 170–179, Number: 3.

[13] William A. Hudson and Mark L. Levin, *Integrated aircraft fuel thermal management system*, October 1988, Inventors: _:n1005 Issue: US4776536A.

[14] JetCat, *P300-PRO*, October 2021.

[15] ———, *P1000-PRO - JetCat*, January 2022.

[16] ———, *P250-Pro-S - JetCat*, January 2022.

[17] ———, *P400-PRO-LN - JetCat*, January 2022.

[18] Rabi Karaali and İlhan Öztürk, *Efficiency improvement of gas turbine cogeneration systems*, Tehnicki vjesnik - Technical Gazette **24** (2017), no. Supplement 1 (en), Number: Supplement 1.

[19] Sanford A. Klein and Gregory Nellis, *Thermodynamics*, Cambridge University Press, New York, 2012, OCLC: ocn701242196.

[20] George Marin, Dmitrii Mendeleev, Boris Osipov, and Azat Akhmetshin, *Study of the effect of fuel temperature on gas turbine performance*, E3S Web of Conferences **178** (2020), 01033 (en).

[21] Jack D. Mattingly, *Elements of propulsion: gas turbines and rockets*, AIAA education series, American Institute of Aeronautics and Astronautics, Reston, Va, 2006, OCLC: ocm69671927.

[22] Jack D Mattingly, William H Heiser, David T Pratt, and ProQuest (Firm), *Aircraft engine design*, American Institute of Aeronautics and Astronautics, Reston, Va., 2002 (English), OCLC: 1261988470.

[23] Donna Mohr, *Statistical methods*, 4 ed., Elsevier, Inc, Philadelphia, 2021.

[24] NIST, *Dodecane*, Publisher: National Institute of Standards and Technology.

[25] PBS Aerospace, *PBS TJ100P: New engine model for tactical UAVs, drones, and missiles*, December 2020.

[26] Élodie Roux (ed.), *Turbofan and turbojet engines: database handbook*, Editions Elodie Roux, Blagnac, 2007 (fre).

[27] Arun K Sehra and Jaiwon Shin, *Revolutionary Propulsion Systems for 21st Century Aviation*, (2003), 13 (en).

[28] Claire Soares, *Gas Turbines*, Gas Turbines, Elsevier, 2015, pp. 1–40 (en).

[29] A. Tourlidakis and A. Malkogianni, *Influence of the Air Preheat Temperature and the Fuel Preheat Temperature in the Adiabatic Flame Temperature for Gaseous Fuels of Low Heating Value*, Volume 1: Aircraft Engine; Ceramics; Coal, Biomass and Alternative Fuels; Controls, Diagnostics and Instrumentation (Copenhagen, Denmark), American Society of Mechanical Engineers, June 2012, pp. 711–719.

[30] KingTech Turbines, *KingTech Turbines Engine Manual, Gen. 4*, September 2021.

[31] VELO3D, *Sierra Turbines Drives Innovation for Microturbines*, (2020), 6 (en).

[32] Heather K. Wiest and Stephen D. Heister, *Experimental Study of Gas Turbine Combustion With Elevated Fuel Temperatures*, Journal of Engineering for Gas Turbines and Power **136** (2014), no. 12, 121507 (en), Number: 12.

[33] Yunus A. Çengel and John M. Cimbala, *Fluid mechanics: fundamentals and applications*, McGraw-Hill series in mechanical engineering, McGraw-HillHigher Education, Boston, 2006.

[34] Yunus A. Çengel and Afshin J. Ghajar, *Heat and mass transfer: fundamentals & applications*, fifth edition ed., McGraw Hill Education, New York, NY, 2015, OCLC: ocn870517093.

VITA

Joshua Robert Braun

Candidate for the Degree of

Master of Science

Thesis: DESIGN AND EVALUATION OF A THERMAL NOZZLE FOR SMALL-SCALE TURBOJETS

Major Field: Mechanical & Aerospace Engineering

Biographical:

Education:

Completed the requirements for the Master of Science in Mechanical & Aerospace Engineering at Oklahoma State University, Stillwater, Oklahoma in May, 2022.

Completed the requirements for the Bachelor of Science in Engineering at Oral Roberts University, Tulsa, Oklahoma in 2016.